Dalton Transactions

ROYAL SOCIETY OF CHEMISTRY

PAPER

View Article Online
View Journal

Cite this: DOI: 10.1039/d6dt00710d

Glycoconjugated $Re(CO)_3^+$ complexes: syntheses, characterization, cytotoxicity and cellular localization

Bita Abdolahi Sanati,[a] Ewan L. Gilleard,[a] Tamara Teixeira,[b] Malgorzata Korbas,[c] Yasuhiro Niwa,[d] Arvi Rauk,[a] Fillipe Vieira Rocha[b] and Farideh Jalilehvand*[a]

Rhenium tricarbonyl complexes with the general formula *fac*-$[Re(CO)_3(N,N')L]^{0/+}$ (where *N,N'* = a bidentate polypyridyl ligand and L = a monodentate axial ligand) have been recognized over the past decade as potential anticancer therapeutics. In the present study, we introduced glycoconjugated diimine ligands into such complexes to enhance their water solubility, biocompatibility and bioavailability, and to target the overexpressed glucose transporters (GLUTs) on cancer cells. We prepared a series of water-stable Re(I) complexes (**1–4**) with the general formula $[Re(CO)_3(N,N')L](CF_3SO_3)$, where *N,N'* = a glycoconjugated diimine (GluP, GluQ, and AcGluP) and L = imidazole (HIm) or indazole (HIn), and tested their *in vitro* cytotoxicity against a series of cancer cell lines. All complexes were characterized using electrospray ionization mass spectrometry, NMR spectroscopy and X-ray absorption spectroscopy. The structure of the diimine ligand (*N,N'*) and the lipophilicity of the complexes were varied, *e.g.* by protecting the hydroxyl (–OH) groups of the glucose moiety with acetyl groups in complex **4**, *fac*-$[Re(CO)_3(\beta\text{-AcGluP})(HIn)](CF_3SO_3)$, to compare potential GLUT-mediated transport *versus* passive diffusion uptake. *In vitro* cytotoxicity results revealed that the more lipophilic complexes **3**, *fac*-$[Re(CO)_3(GluQ)(HIn)](CF_3SO_3)$, and **4** have moderate cytotoxicity. X-ray fluorescence microscopy (XFM) allowed us to evaluate the cellular distribution of complexes **3** and **4** in A2780 ovarian cancer cells. Complex **3**, which has unprotected sugar –OH groups, accumulated more in the nuclear/perinuclear area. In contrast, the more lipophilic complex **4** showed lower Re accumulation and a more uniform intracellular distribution. For the non-cytotoxic hydrophilic complex **1**, *fac*-$[Re(CO)_3(GluP)(HIm)](CF_3SO_3)$, XFM showed a much weaker intracellular Re signal, while ICP-MS detected significant uptake by HepG2 liver cancer cells. The observations suggest partial involvement of glucose transport pathways in the uptake of complexes **1** and **3**.

Received 26th March 2026,
Accepted 15th May 2026

DOI: 10.1039/d6dt00710d

rsc.li/dalton

1. Introduction

Transition metal complexes have been important in the field of medicinal chemistry since the FDA approval of cisplatin as an anticancer drug in 1978.[1] Cisplatin and its analogues are known to mainly target DNA *via* interaction with purine bases, leading to apoptosis in malignant cells.[1–3] Later, cisplatin analogue complexes such as carboplatin, oxaliplatin, and heptaplatin have been developed to overcome some limitations of cisplatin such as dose-limiting toxicity and drug resistance.[1,4,5] The high potency and cytotoxicity of these anticancer complexes have made them desirable; however, they still often lack selectivity and stability in biological media, leading to toxic side effects. In the past two decades, complexes of aluminum(I), iron(II), copper(II), ruthenium(II & III), palladium(II), gadolinium(III), and gold(I & III) have been investigated for their anticancer properties and some have successfully entered clinical trials; however, their selectivity towards cancer cells has largely remained unattained.[6–13]

The limitations of current successful Pt(II) anticancer agents have shifted research towards transition metal complexes with increased selectivity towards cancer cells, while maintaining their structural integrity to prevent off-target side effects. One way to enhance the selectivity of an anticancer compound is to target specific cellular transporters such as glucose transporters (GLUTs) that are overexpressed on cancer cells. This is due to the increased rate of glucose consumption by these malignant cells, which exhibit increased metabolic activity.[14] GLUTs have been previously targeted by ^{18}F-fluorodeoxyglucose (^{18}F-FDG), which is commonly used in positron

[a]*Department of Chemistry, University of Calgary, Calgary T2N 1N4, Alberta, Canada. E-mail: faridehj@ucalgary.ca*
[b]*Department of Chemistry, Federal University of São Carlos, São Carlos 13565-905, São Paulo, Brazil*
[c]*Argonne National Laboratory, Lemont 60439, Illinois, USA*
[d]*Photon Factory, Institute for Materials Structure Science, High Energy Accelerator Research Organization, Tsukuba 305-0801, Japan*

emission tomography (PET) and is readily taken up by cancer cells.[15] Glucose-containing analogues of cisplatin and other platinum complexes (Scheme 1) have also been reported to show preferential cellular uptake in cancer cells.[16,17] More specifically, complexes bearing a glucose moiety conjugated *via* carbon 2 (C_2) have been shown to be most efficiently internalized by GLUT-1 proteins.[18] In this process, it is important for the glucose moiety to remain attached to the drug/metal center until reaching the GLUT target. Kinetically inert transition metal centers like the rhenium(I) ion are then favorable for avoiding rapid ligand substitution.

Rhenium(I) tricarbonyl complexes, *fac*-$[Re(CO)_3(N,N')L]^{0/+}$, where (*N*,*N*′) is a bidentate diimine and L is a monodentate ligand, have been investigated for their anticancer and photophysical activities. The low spin d^6 electronic configuration of the $Re(CO)_3^+$ entity often promotes inertness in solution and makes it favorable for designing photo-CORMs (photo-activated CO releasing molecules), *i.e.* $Re(CO)_3^+$ complexes that can release toxic CO molecules upon irradiation with light of specific energy and are otherwise nontoxic.[19–21] Others have been reported to target different organelles in cancer cells such as mitochondria and affect the levels of reactive oxygen species in their target cells.[22,23] The axial (L) ligand of early *fac*-[Re$(CO)_3(N,N')L$] complexes was often a halide such as Cl or Br, which would form neutral species.[24–27] However, the halide ligand would undergo ligand substitution with solvent molecules such as H_2O upon solvation, forming a *fac*-$[Re(CO)_3(N,N')(H_2O)]^+$ complex.[28,29] Such rapid substitution *in vivo* before reaching the target could lead to undesired interactions and increased toxic side effects, as observed for cisplatin.[1] Thus, it is important to design anticancer complexes that maintain their integrity before reaching their target. An example of such a complex is *fac*-[Re$(CO)_3$(2,9-dimethyl-1,10-phenanthroline)(*p*-tolylisonitrile)]$^+$, in which the coordination environment remained intact as monitored by X-ray fluorescence microscopy.[30,31] Furthermore, *fac*-[Re$(CO)_3(N,N')L]^+$ complexes bearing (*N*,*N*′) = 1,10-phenanthroline (phen) and 2,2′-bipyridine (bpy), and N-donor axial ligands such as substituted pyridine were reported to show *in vitro* and *in vivo* cytotoxicity against a series of cancer cell lines (Scheme 2). These complexes are also shown to target subcellular organelles such as mitochondria and lysosomes.[23,32–35]

The diimine ligand in *fac*-$[Re(CO)_3(N,N')L]^{0/+}$ complexes is often a polypyridyl group such as bpy or phen. These ligands are not biocompatible, and their complexes often lack solubility in aqueous media. Using a diimine ligand bearing a glucose moiety would enhance the solubility and biocompatibility of its $Re(CO)_3^+$ complexes while targeting GLUTs. Such glycoconjugated rhenium(I) tricarbonyl complexes were initially introduced as analogues of their $^{99m}Tc(CO)_3^+$ radiopharmaceutical complexes that were designed for diagnostic and therapeutic purposes.[36] However, the carbohydrate moiety in these complexes was often conjugated *via* a linker due to the instability and weaker coordination ability of the sugar hydroxyl (–OH) groups.[37]

Our goal in the present study was to prepare stable *fac*-[Re$(CO)_3(N,N')L]^+$ complexes bearing glucose-derived ligands and evaluate how ligand design influences their stability, lipophilicity, cellular uptake, and biological activity in cancer cells. As such, we selected glucose containing diimine ligands (*N*,*N*′ = GluP and GluQ; Scheme 3), which can be readily obtained by condensation of an amino sugar, *e.g.* D-glucosamine, with an aromatic aldehyde such as 2-pyridinecarboxaldehyde. This design was based on the rationale that the presence of a glucose-derived moiety could potentially influence cellular uptake, although no specific transport mechanism was examined in this study. As the axial L group, we chose imidazole, a naturally abundant N-donor ligand, or indazole, which is used in some FDA-approved anticancer drugs.[38] Both imidazole and indazole were also used in the well-known ruthenium-based anticancer complexes, NAMI-A, KP1019 and NKP-1339 (BOLD-100); the latter is currently in clinical trials.[7,39,40]

We also considered that, if direct participation of glucose transport pathways proved limited, increasing lipophilicity might favor cellular uptake through non-specific membrane permeation. For that purpose, we also prepared a $Re(CO)_3^+$ complex of the AcGluP ligand, in which all –OH groups were acetylated (Scheme 3). There has been a report on acetylated glucose moieties enhancing the antitumor activity of a gold(I) complex *in vivo*.[41]

Thus, we synthesized glycoconjugated $Re(CO)_3^+$ complexes **1**–**4** (Scheme 3) and tested their cytotoxicity towards a series of cancer cells and a primary (non-cancerous) cell line. Elemental distribution maps and cellular localization of these complexes were obtained for a selected cancer cell line through X-ray Fluorescence Microscopy (XFM), revealing the extent to which they could be taken up by the cells. The effect of the most cytotoxic complex on cell morphology was evaluated by monitoring the A2780 cells after exposure to different concentrations of complex **4**. Furthermore, the clonogenic assay was performed to test whether this complex exhibited any cytostatic activity.

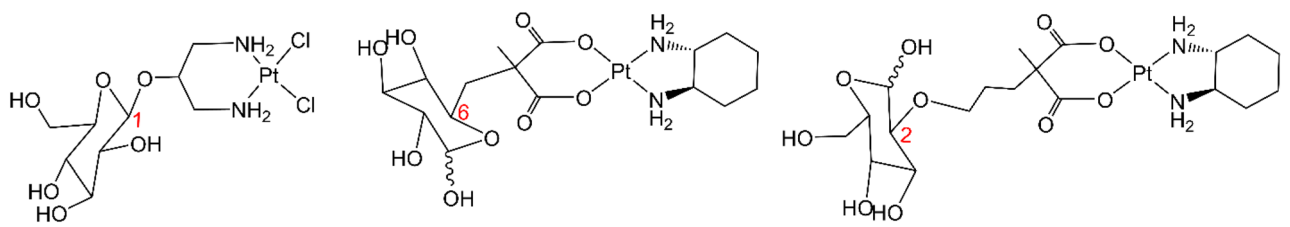

Scheme 1 Structures of reported glucose-containing platinum anticancer complexes.[16–18]

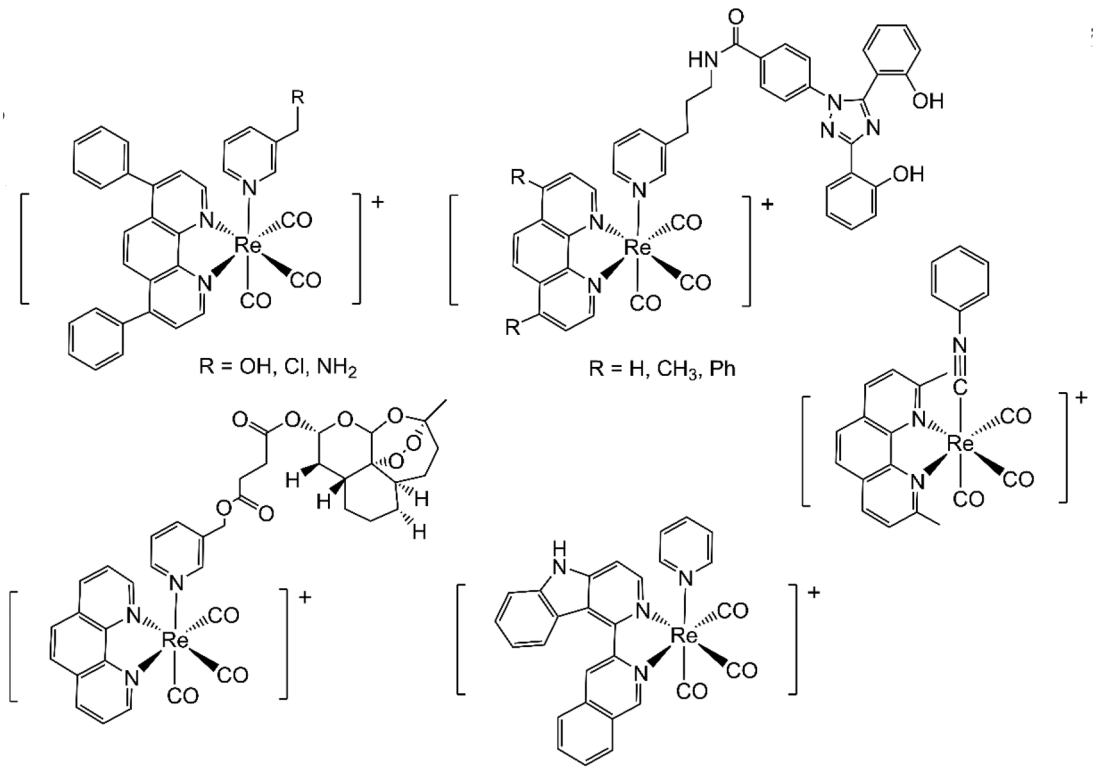

Scheme 2 Structures of anticancer *fac*-$[Re(CO)_3(N,N')L]^+$ complexes bearing (*N*/*C*)-donor axial ligands.[23,32–34]

2. Results and discussion

With the goal of preparing water-soluble, stable anticancer *fac*-$[Re(CO)_3(N,N')L]^+$ complexes that could be preferentially taken up by cancer cells with GLUT-1 overexpression, we initially synthesized the *fac*-$[Re(CO)_3(GluP)Cl]$ compound containing the glycoconjugated (*N*,*N*′) ligand GluP (Scheme 3). Its structural characterization using NMR spectroscopy showed that, depending on the relative orientation of the GluP sugar entity towards Cl, this compound exists as a pair of diastereomers, each with α (minor) and β (major) anomers, and could undergo complete hydrolysis in aqueous solution over 48 h, forming *fac*-$[Re(CO)_3(GluP)(H_2O)]Cl$. Moreover, a small fraction (<1%) of the compound in the form of the *fac*-$[Re(CO)_3(\alpha\text{-GluP})Cl]$ isomer could lose a CO ligand in protic solvents under ambient conditions.[28]

We then prepared a series of $Re(CO)_3^+$ glycoconjugated compounds by substituting the axial group with the N-donor ligands imidazole (HIm) and indazole (HIn) in *fac*-$[Re(CO)_3(GluP)(HIm)](OTf)$ (**1**) and *fac*-$[Re(CO)_3(GluP)(HIn)](OTf)$ (**2**); ($OTf^- = CF_3SO_3^-$). We also enhanced the lipophilicity of the glycoconjugated ligand by replacing GluP with GluQ and AcGluP (Scheme 3) in *fac*-$[Re(CO)_3(GluQ)(HIn)](OTf)$ (**3**) and *fac*-$[Re(CO)_3(AcGluP)(HIn)](OTf)$ (**4**) to promote the cellular uptake of these compounds through passive diffusion and compared the cytotoxicity of these glycoconjugated compounds (**1–4**).

2.1. Syntheses and characterization

The diimine ligands GluQ and AcGluP were synthesized by condensing an amino sugar with an aromatic aldehyde, using a mild base (triethylamine, NEt_3) to neutralize the hydrochloride salt (Scheme 4).[42,43] The purity of these ligands, which are stable at room temperature for weeks when stored in a desiccator under low pressure, was confirmed by elemental analysis and NMR spectroscopy (Fig. S1a–S2a). The formation of GluP in **1** and **2** occurred *in situ* in a one-pot synthesis (Scheme 5), since GluP is highly sensitive to moisture at room temperature[44] and should be used as soon as it is prepared.

The compounds *fac*-$[Re(CO)_3(GluP)Cl]$,[28] *fac*-$[Re(CO)_3(GluQ)Cl]$, and *fac*-$[Re(CO)_3(AcGluP)Cl]$ were initially prepared as precursors to complexes **1** and **2**, **3**, and **4**, respectively. Then the precursors were reacted with $Ag(CF_3SO_3)$ to prepare the intermediate *fac*-$[Re(CO)_3(N,N')(CF_3SO_3)]$ complex, in which the weakly coordinating triflate ($OTf^- = CF_3SO_3^-$) was replaced by the N-donor ligands imidazole (HIm) and indazole (HIn), resulting in *fac*-$[Re(CO)_3(GluP)(HIm)](OTf)$ (**1**), *fac*-$[Re(CO)_3(GluP)(HIn)](OTf)$ (**2**), *fac*-$[Re(CO)_3(GluQ)(HIn)](OTf)$ (**3**), and *fac*-$[Re(CO)_3(AcGluP)(HIn)](OTf)$ (**4**) (Scheme 5).

The triflate compounds of complexes **1–4** were purified using Sephadex LH-20 size exclusion chromatography; in each case the purity of the main band was checked using high-resolution ESI-mass spectrometry to ensure the absence of the free ligand or reaction by-products (Fig. S7 and S8). After eva-

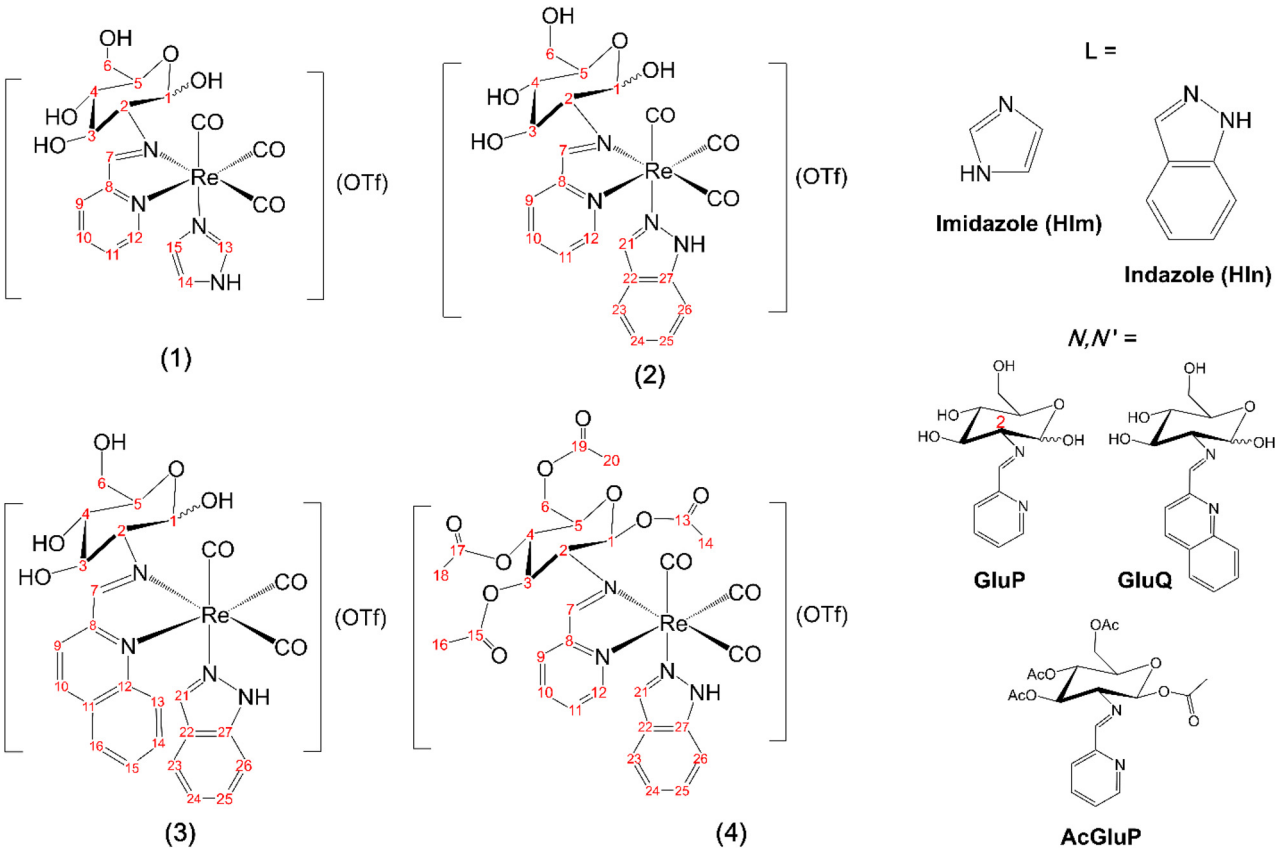

Scheme 3 Re(I) glycoconjugated complexes in this work: *fac*-[Re(CO)$_3$(GluP)(HIm)](CF$_3$SO$_3$) (**1**), *fac*-[Re(CO)$_3$(GluP)(HIn)](CF$_3$SO$_3$) (**2**), *fac*-[Re(CO)$_3$(GluQ)(HIn)](CF$_3$SO$_3$) (**3**), and *fac*-[Re(CO)$_3$(AcGluP)(HIn)](CF$_3$SO$_3$) (**4**), their axial ligands (L = imidazole and indazole), and the diimine (*N*,*N*′) ligands GluP, GluQ and AcGluP.

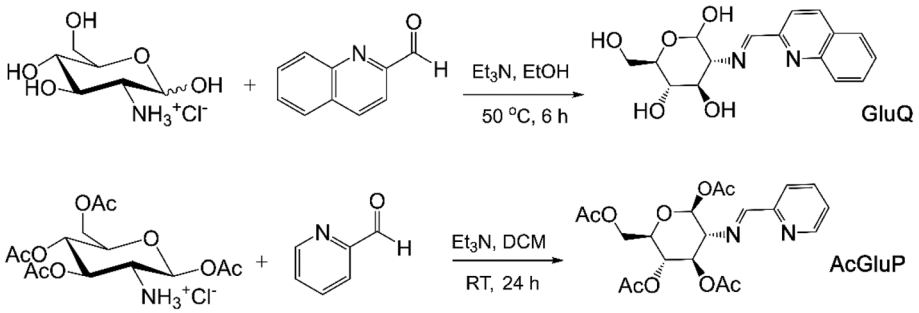

Scheme 4 Syntheses of the glycoconjugated ligands GluQ and AcGluP.[42,43]

porating the main band to dryness, the purity of the compound was confirmed *via* elemental analysis (**1** and **4**) and/or ^{1}H NMR spectroscopy (Fig. S3a–S6a). Furthermore, the facial arrangement of the CO ligands was confirmed by measuring their FT-IR spectra (Fig. S9).

Complexes **1** and **2** are highly soluble in water, while the limited water solubility of complex **3** (~1 mM) is still sufficient for biological assays, UV-vis and ^{1}H NMR spectroscopy (Fig. S5c). Complex **4** dissolves in aqueous solutions containing 0.5–2% methanol or 3–5% acetone, depending on the concentration needed for biological assays or UV-vis measurements. To obtain the ^{1}H NMR spectrum of **4** (~6 mM) in D_2O, 10% CD_3OD was needed (Fig. S6c).

NMR spectroscopy. Complexes **1–3** bearing unprotected sugar –OH groups allow for free tautomerization at the anomeric carbon (C_1-OH) in solution, in which the D-glucopyranose ring opens and closes to form two anomers, *i.e.*, α and β anomers. However, the acetylation of the D-glucopyranose rings in complex **4** prevents tautomerization and only the β anomer is observed (Scheme 6). The β anomer is typically the

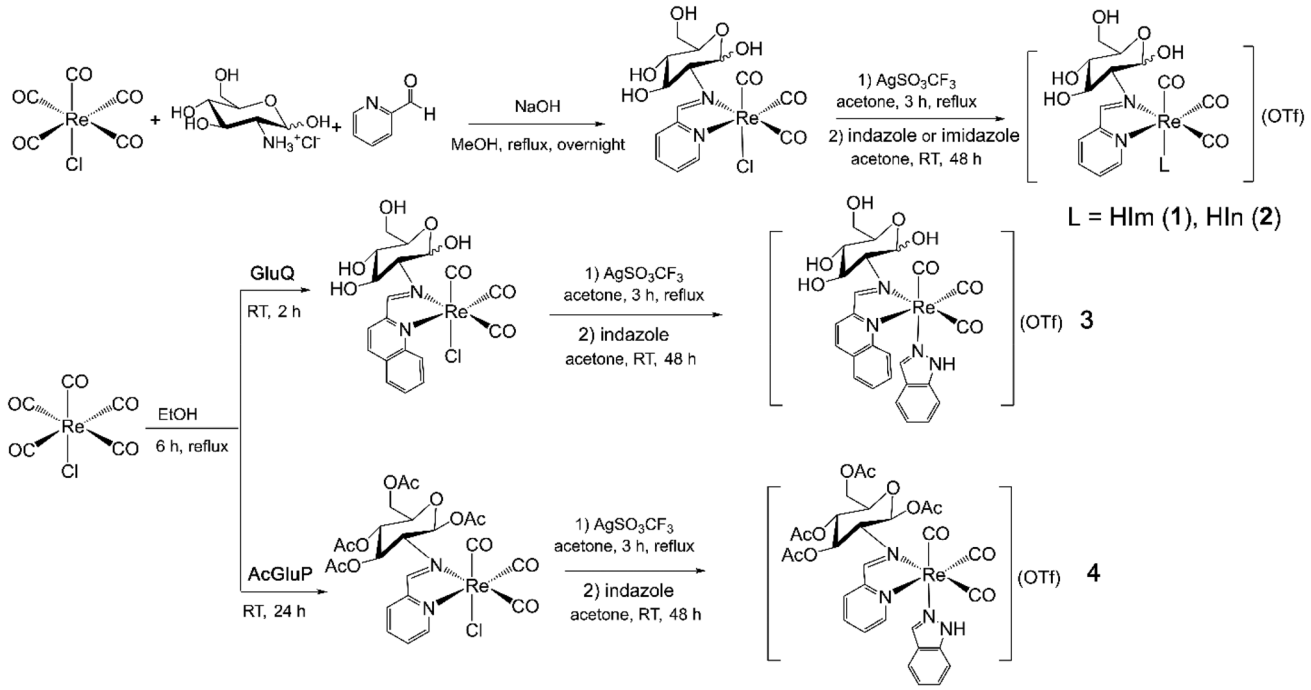

Scheme 5 Synthetic route for preparing complexes **1–4**.

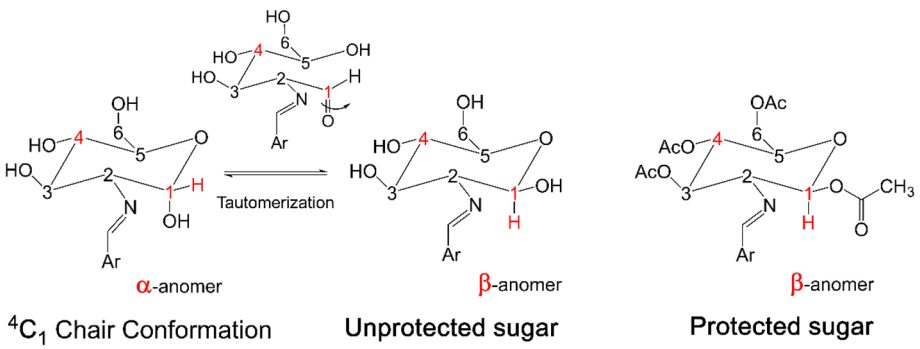

Scheme 6 Tautomerization of D-glucopyranose in the $^4C_1$ chair conformation (left panel) does not occur in acetylated D-glucopyranose (right panel).

major species in polar solvents due to the favorable hydrogen bonding of the equatorial –OH groups with protic solvent molecules.[45] Moreover, in the α anomer the intramolecular hydrogen bonding between the imine nitrogen and the axial –OH prevents the *exo*-anomeric effect (*i.e.*, $n_{O_1} \rightarrow \sigma^*_{C_1-O_5}$ stabilizing orbital interaction),[46] leading to preferential formation of the β anomer in polar solvents. Note that the D-glucopyranose ring only adopts the $^4C_1$ chair conformation based on the ^{1}H NMR coupling constants of C_1H and C_2H, which are $^3J_{HH}$ = 2–4 Hz (α) and 6–9 Hz (β).[46]

All complexes have two sets of signals per anomer that are more apparent in the anomeric region of the ^{1}H NMR spectra of complexes **1** and **2** (Fig. S3a–S4a), *i.e.*, two α anomer and two β anomer signals. For complex **3** these signals are merged, showing one peak for α anomers and one peak for β anomers (Fig. S5a). Only two β-anomer peaks are observed for complex **4** (Fig. 1). The presence of two diastereomers is due to the chirality of the Re(I) center, which was also observed for the precursor *fac*-[Re(CO)$_3$(GluP)Cl], as discussed previously.[28] Theoretical studies confirmed the existence of two diastereomers for complexes **1–4** (see below).

In the ^{13}C NMR spectra of complexes **1–4**, the signals for the carbonyl ligands were observed in the 180–200 ppm range (see Fig. S3a–S6a) and resemble the facial rhenium tricarbonyl isomer based on their longer NMR relaxation time compared to the meridional isomer.[25] Due to the low intensity of these facial quaternary carbons, the α-anomer carbonyls in complexes **1–3** were not easy to detect because of their lower concentration.

Theoretical calculations. Ground state density functional theory (DFT) calculations were carried out to predict the struc-

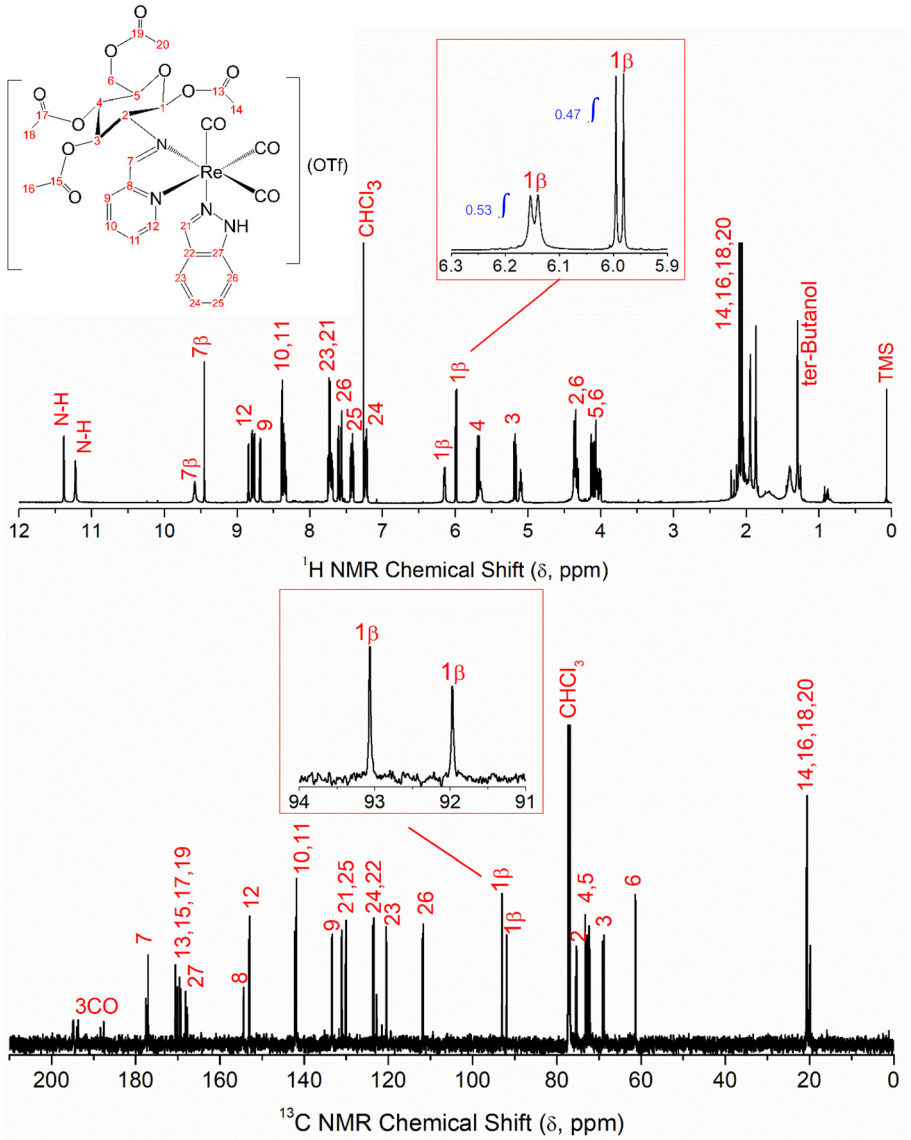

Fig. 1 ^{1}H and ^{13}C NMR spectra (600 MHz, 25 °C, $CDCl_3$) of *fac*-[$Re(CO)_3$(AcGluP)(HIn)](OTf) (**4**). Inset: Anomeric region showing two distinct signals for the C_1H_β anomers with a diastereomeric ratio of 0.9; see also Fig. S6a. The ^{1}H NMR spectrum in D_2O (+10% CD_3OD) is shown in Fig. 8 and Fig. S6c.

tures and optimize the geometries of the GluP, GluQ and AcGluP ligands and their corresponding glycoconjugated rhenium tricarbonyl complexes **1–4**; for details see the SI. The existence of the two diastereomers for each complex was confirmed through the two different orientations of the glycoconjugated ligand towards the $Re(CO)_3^+$ entity and the axial ligand. Depending on whether the sugar's C_1 or C_3 atom is facing the axial ligand, different intramolecular interactions can take place, resulting in two distinct ground state structures (structures **A** and **B** in Fig. 2 and Table S1d).

For example, according to the ^{1}H NMR spectrum shown in Fig. 1, *fac*-[$Re(CO)_3$(AcGluP)(HIm)](OTf) (**4**) has two β anomers with similar concentrations. Assuming these structures are in equilibrium but exchange slowly on the NMR time scale, their diastereomeric ratio was determined to be 0.9 based on their ^{1}H NMR peak integrals (Fig. 1 and Table S1c). The corresponding ΔG value is ~0.3 kJ mol^{-1}, calculated according to the Gibbs free energy equation, $\Delta G = -RT \ln K$, where K is the equilibrium constant, *i.e.* in this case, the ratio of the two β anomers, T = 298 K, and R = 8.314 × 10^{-3} kJ mol^{-1} K^{-1}. The DFT calculated Gibbs free energy difference between these two β anomers in water (SMD solvent corrected) is $\Delta(\Delta G^*)$ ~−14 kJ mol^{-1} (Table S1c). Using the same equation, this energy difference leads to a diastereomeric ratio of 284, favouring one of the diastereomers, as opposed to the experimental ratio of 0.9. The reason for this difference is an error of at least 14 kJ mol^{-1} in calculating $\Delta(\Delta G^*)$ for this complex. This error may be due in part to the SMD solvation model and partly to the lack of accounting for the collective entropy of the ensembles of the two species, which may increase the ΔG difference between

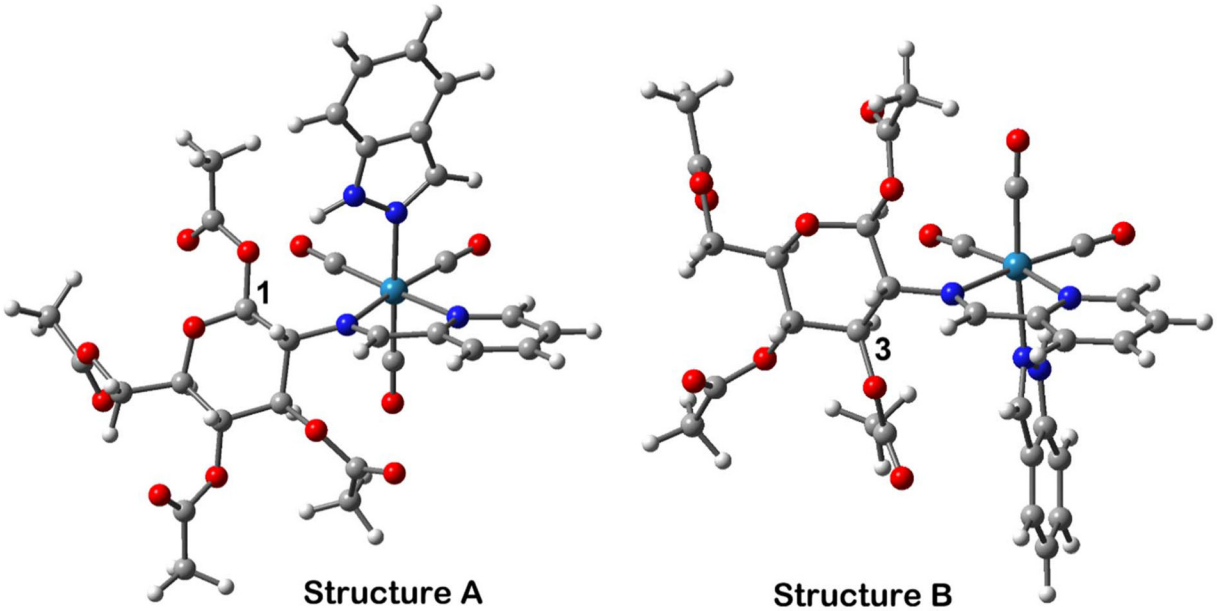

Fig. 2 DFT calculated diastereomers of *fac*-[Re(CO)$_3$(β-AcGluP)(HIn)](OTf) (**4**) showing that in structure **A**, the C$_1$-OAc (acetyl group) faces the axial indazole ligand, while in structure **B**, C$_3$-OAc does. The latter structure has a lower (~14 kJ mol^{-1}) calculated Gibbs free energy in water.

the two diastereomers, contrary to the experimental observations. It should be noted that the ^{1}H NMR signals for each of the β anomers represent a time-average of an ensemble of conformations, and the structures shown in Fig. 2 are the most stable for each species. Given the complexity of the systems, we consider the theoretical calculation results satisfactory.

For compounds **1** and **2** with both α and β anomers, the situation is more complex. Based on the ^{1}H NMR peak integral for each anomer (Fig. S3a and S4a), the experimental ΔG values were found to differ by up to ~20 kJ mol^{-1} from the DFT calculated $\Delta(\Delta G^*)$ ones for each pair of diastereomers (Table S1c). Thus, the DFT calculated diastereomeric ratios differ from those observed in their ^{1}H NMR spectra.

X-ray absorption spectroscopy (XAS). The k^3-weighted Re L$_3$-edge X-ray absorption fine structure (EXAFS) spectra of **1–4** are shown in Fig. 3 along with their corresponding Fourier transforms (not corrected for the phase shift), displaying two main

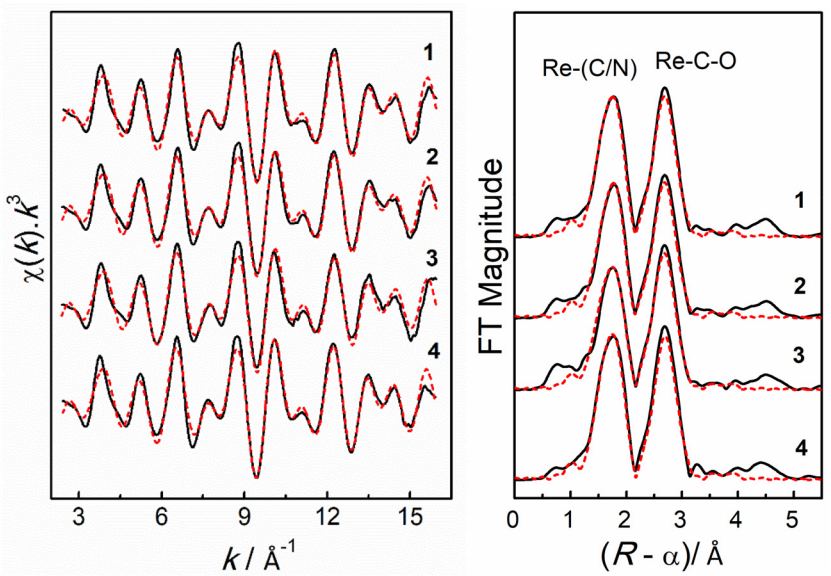

Fig. 3 Least square curve-fitting of k^3-weighted Re L$_3$-edge EXAFS spectra of **1–4** and their corresponding Fourier transform (not corrected for phase shift); see Table 1.

Table 1 Least squares curve fitting results of Re L_3-edge EXAFS spectra shown in Fig. 3 [a]

	Re–C			Re–N			Re–C–O (n_{leg} = 3)		
Complex	N	R (Å)	σ^2 (Å^2)	N	R (Å)	σ^2 (Å^2)	N	R (Å)	σ^2 (Å^2)
1	3*f*	1.92	0.0031	3*f*	2.16	0.0032	6*f*	3.09	0.0020
2	3*f*	1.92	0.0036	3*f*	2.16	0.0030	6*f*	3.09	0.0022
3	3*f*	1.92	0.0038	3*f*	2.16	0.0041	6*f*	3.08	0.0022
4	3*f*	1.92	0.0029	3*f*	2.17	0.0032	6*f*	3.09	0.0019

[a] Fitting k-range = 2.4–15.9 Å^{-1}; f = fixed; estimated errors for the refined parameters: R ± 0.02 Å and σ^2 ± 0.001 Å^2. $S_0{}^2$ value was fixed at 1.0 (transmission data).

peaks at around 1.8 Å and 2.7 Å related to Re–(N/C) and Re–C–O scattering paths (Scheme S1), respectively. The refined distances are nearly identical: Re–C 1.92 ± 0.02 Å, Re–N 2.16 ± 0.02 Å and Re–C–O 3.09 ± 0.02 Å (see Table 1), and are similar to the average bond distances of their corresponding ground state optimized geometries (Re–C 1.93, Re–N 2.23–2.27, and Re–C–O 3.09 Å; see Table S1e). Typically, one cannot differentiate between Re–C and Re–N bond distances because of the similar electron density of these backscattering atoms. However, for this data set with Δk = 12.5 Å^{-1} (the k-range of the collected data), the resolution of distances between the absorber and similar backscattering atoms is $\Delta R = \frac{\pi}{2\Delta k} = 0.13$ Å. Since the difference between the Re–C and Re–N distances is 0.24 Å, their scattering contributions can be refined separately.

Electronic absorption spectroscopy. The electronic absorption spectra of **1–4** display a low energy band at around 330–450 nm (Fig. 4), mainly attributed, based on TD-DFT calculations, to the metal-to-ligand charge transfer (MLCT) or metal–ligand-to-ligand charge transfer (MLLCT) involving mixed Re and ligand HOMOs (Tables S3–S10). The maximum absorption (λ_{max}) of this band displays a red shift as the π conjugation of the diimine (*N*,*N*′) ligand increases from GluP in **2** to GluQ in **3** (λ_{max} = 367 to 403 nm), changing the solution color from yellow (**2**) to orange (**3**). The red shift can be explained based on the stabilization of the π* orbitals through extended π conjugation, leading to lower energy requirements to excite electrons from the MOs on the Re d orbitals to the diimine ligand's π* (LUMO).

Substitution of the axial ligand imidazole in **1** with indazole in **2** leads to a shift of the MLCT band from λ_{max} = 375 to 367 nm (Fig. 4).[47] TD-DFT calculations for the structures with the lowest calculated energies in solvent (structures **A**– β-anomer for **1** and **2**; Table S1d) showed that for complex **1**, the λ = 375 nm band is mainly composed of transitions from (HOMO–2) and (HOMO–1) to the LUMO (Fig. 5). The corresponding band for complex **2** at λ = 367 nm arises from the (HOMO–2) to LUMO transition; see Fig. S12 and S14. Based on these calculations, the L ligands imidazole and indazole are not directly involved in the lowest-energy absorption bands (Fig. S11, S13 and Tables S3–S6), and they have little effect on the overall energy gap between the occupied and unoccupied MOs.

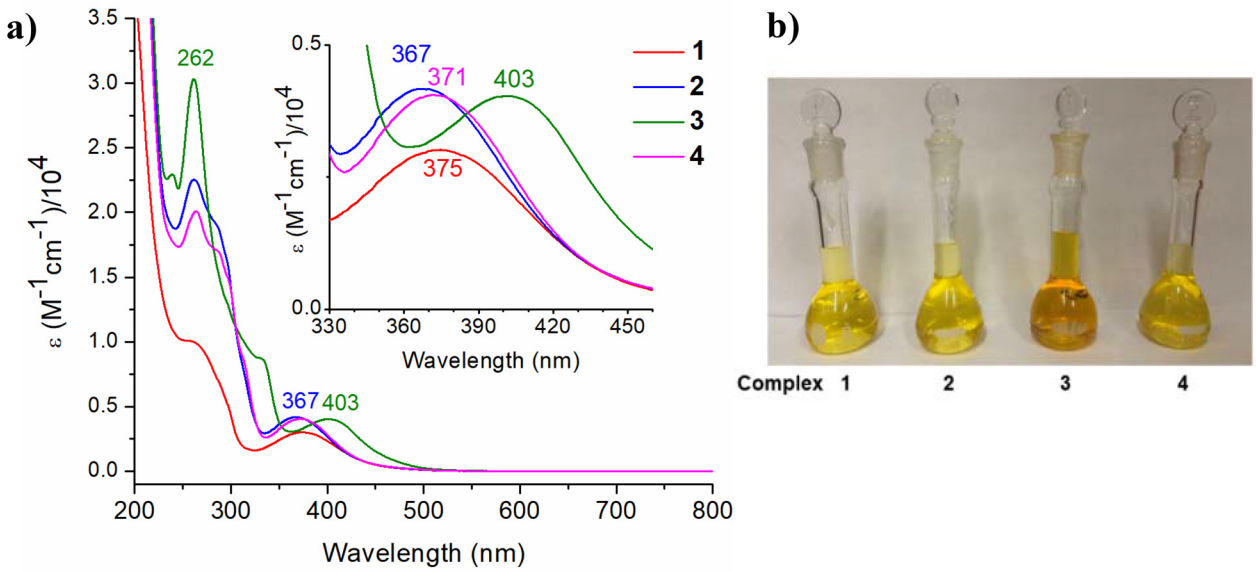

Fig. 4 (a) UV-vis spectra of freshly prepared aqueous solutions (C = 50 μM) of *fac*-[Re(CO)$_3$(GluP)(HIm)](OTf) (**1**), *fac*-[Re(CO)$_3$(GluP)(HIn)](OTf) (**2**), *fac*-[Re(CO)$_3$(GluQ)(HIn)](OTf) (**3**), and *fac*-[Re(CO)$_3$(AcGluP)(HIn)](OTf) (**4**, in 0.5% methanol) and (b) aqueous solutions of complexes **1–4** (C = 1.0 mM).

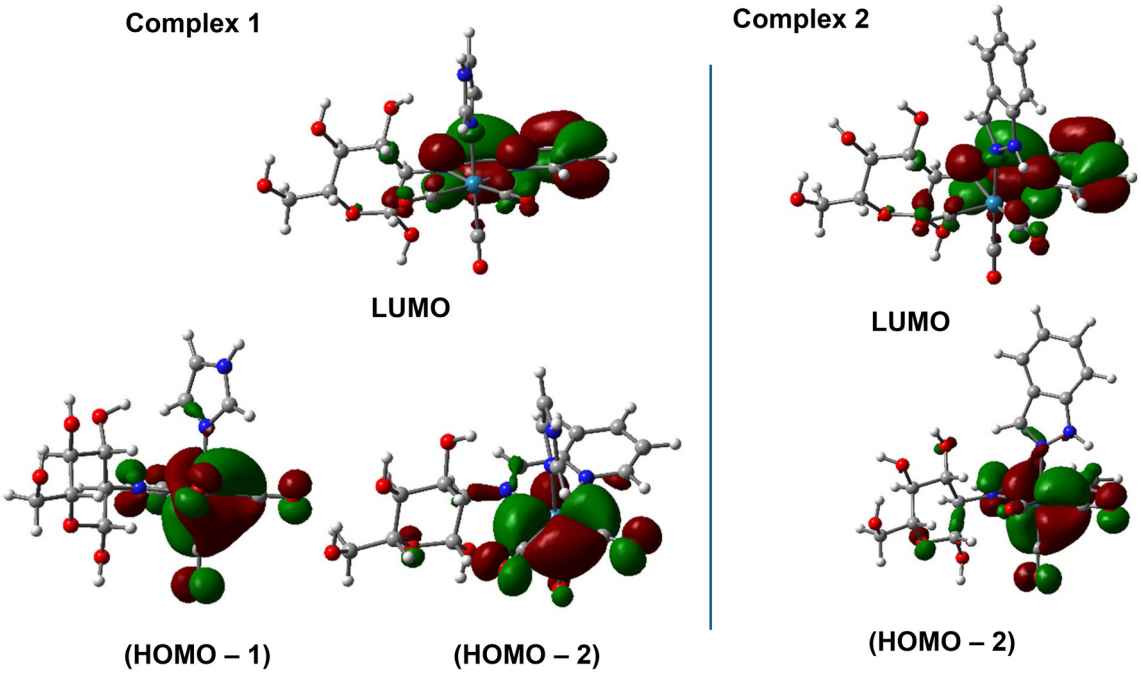

Fig. 5 DFT calculated HOMOs and LUMOs of structures in a solvent with the lowest calculated energy: (left panel) *fac*-[Re(CO)$_3$(β-GluP)(HIm)](OTf) (**1**) and (right panel) *fac*-[Re(CO)$_3$(β-GluP)(HIn)](OTf) (**2**) (structures **A**–βanomer in Table S1d), showing Re–CO (CO π*) orbitals as HOMOs and GluP conjugation π* orbitals as LUMOs. Transitions between these orbitals (LMCT) are observed as peaks at λ_{max} = 375 nm and 367 nm for **1** and **2**, respectively.

2.2. Aqueous stability

The electronic absorption spectra of aqueous solutions (50 μM) of *fac*-[Re(CO)$_3$(GluP)(HIm)](OTf) (**1**) and *fac*-[Re(CO)$_3$(GluP)(HIn)](OTf) (**2**) monitored over 72 h exhibited no change (Fig. S19), and their pH values varied only slightly (5.6–6.1 for **1** and 5.3–5.5 for **2**). Meanwhile the absorption spectra of *fac*-[Re(CO)$_3$(GluQ)(HIn)](OTf) (**3**) and *fac*-[Re(CO)$_3$(AcGluP)(HIn)](OTf) (**4**) displayed a minor decrease over time, with pH remaining within a narrow range of 5.4–5.5 for **3** and 5.5–5.9 for **4** (Fig. 6).

In the ESI-mass spectra of complexes **1**–**3** in aqueous solution, a peak associated with the dicarbonyl species [Re(CO)$_2$(GluP/GluQ)L]$^+$ appears (+*m*/*z* = 579.088, 629.104, and 679.121 amu for **1**, **2** and **3**, respectively); see Fig. S7a, S8a and Fig. 7. Formation of dicarbonyl species was not observed for the *fac*-[Re(CO)$_3$(AcGluP)(HIn)](OTf) (**4**) complex, since the hydroxyl groups in AcGluP are protected through acetylation

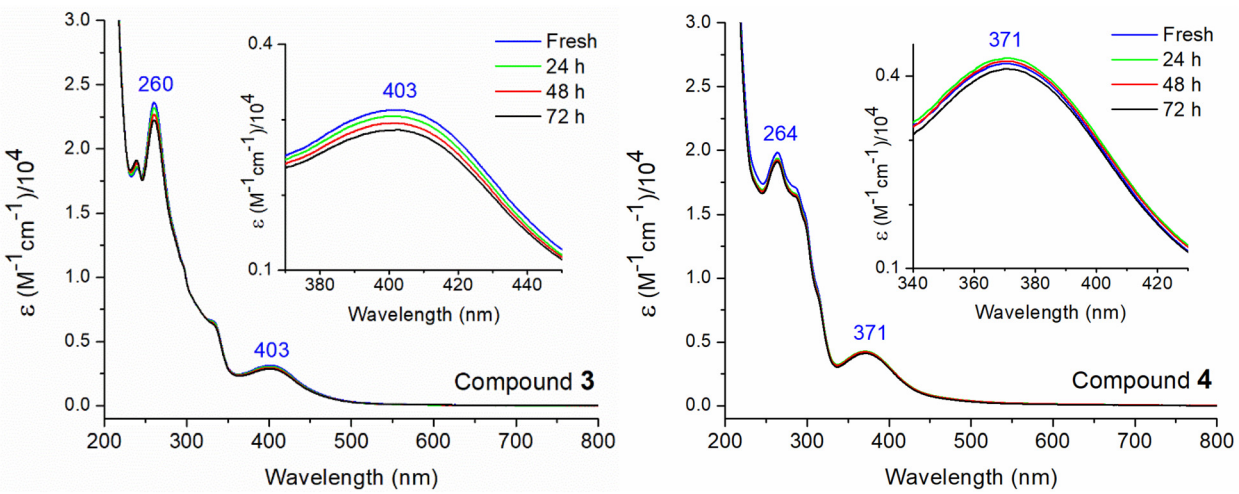

Fig. 6 UV-vis spectra of a 50 μM aqueous solution of*fac*-[Re(CO)$_3$(GluQ)(HIn)](OTf) (**3**) and *fac*-[Re(CO)$_3$(AcGluP)(HIn)](OTf) (**4**; with 0.5% methanol) over 72 h.

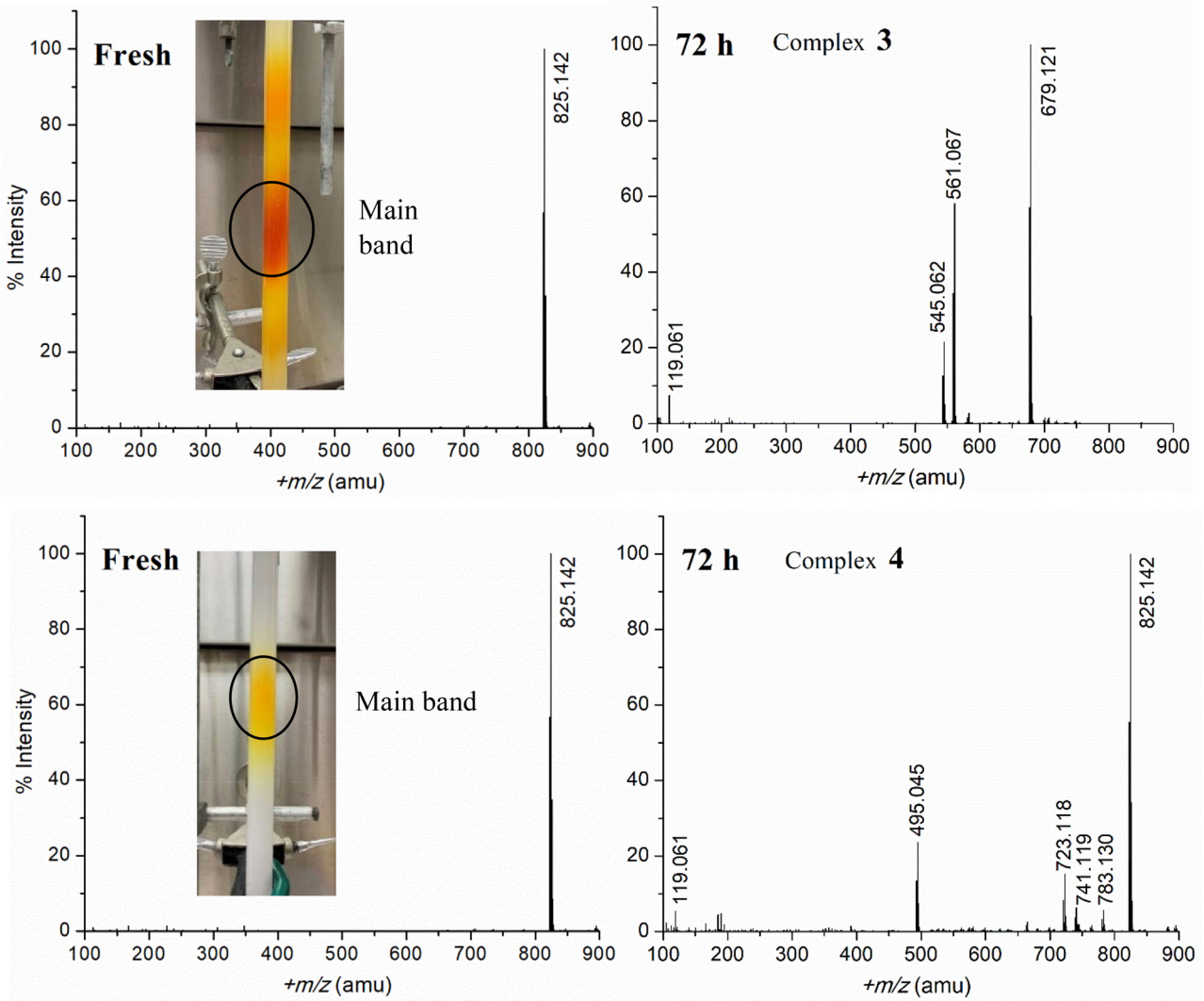

Fig. 7 ESI-mass spectra (+ion mode) of (top panel) *fac*-[Re(CO)$_3$(GluQ)(HIn)](OTf) (**3**) in water, and (bottom panel) *fac*-[Re(CO)$_3$(AcGluP)(HIn)](OTf) (**4**) in water + 0.5% methanol, freshly dissolved and after 72 h. The size exclusion chromatography columns used for purification, and the collected main bands are shown on the left.

and are therefore unavailable for coordination to the Re(CO)$_3^+$ entity by displacing one of the coordinated equatorial CO ligands.[28] For quantitative measurement of the CO loss of **2** and **3** in aqueous solution, gas chromatography coupled with thermal conductivity detection (GC-TCD) was used, showing the release of an insignificant amount of CO gas (<0.1%, see the SI), even though the peak for the [Re(CO)$_2$(GluQ)(HIn)]$^+$ mass ion at +*m*/*z* = 679.121 in the spectrum of **3** (72 h in Fig. 7) showed a 100% relative intensity, evidence that ESI-MS is not a quantitative technique. Such spontaneous CO release (<1%) was initially detected for *fac*-[Re(CO)$_3$(α-GluP)Cl].[28]

The presence of mass peaks at +*m*/*z* = 119.061 and 561.067 amu in the ESI-mass spectrum of complex **3** recorded after 72 h (Fig. 7), which correspond to the protonated indazole and [Re(CO)$_2$(GluQ)]$^+$ ions, respectively, could be attributed to partial dissociation of the axial indazole ligand from this complex in aqueous solution and may explain the minor loss of intensity observed in the UV-vis spectrum of complex **3** over 72 h (Fig. 6). Slight changes in the UV-vis absorption of complex **4** could also be due to the potential loss of the AcGluP ligand, based on a minor peak at +*m*/*z* = 495.045 amu in its ESI-mass spectrum, or due to the hydrolysis of one or two acetyl groups in aqueous solution within 72 h, based on the small mass peaks observed at +*m*/*z* = 723.118, 741.119 and 783.130 amu (Fig. 7 and Table 2).

Partial hydrolysis of the AcGluP acetyl groups was further confirmed through a ^{1}H NMR time study of complex **4** in D$_2$O (+10% CD$_3$OD) over 72 h, which showed a small peak at 2.08 ppm that gradually increased in intensity over time (Fig. 8, right). Although this peak has been assigned to acetic acid,[48] considering the pD = 6.61 of this solution (pD = pH reading + 0.4),[49] the peak is, in this case, associated with the acetate (CH$_3$COO$^-$) group,[50] resulting from partial deacetylation of AcGluP upon reaction with HOD/D$_2$O.[51] It is note-

Table 2 ESI-mass peak assignments of complexes **3** and **4** shown in Fig. 7

+*m*/*z*	Peak assignment[a]
Complex 3	
119.061	$[HIn + H^+]^+$ (calc. = 119.061)
561.067	$[Re^+ + 2CO + GluQ]^+$ (calc. = 561.067)
679.121	$[Re^+ + 2CO + GluQ + HIn]^+$ (calc. = 679.120)
707.114	$[Re^+ + 3CO + GluQ + HIn]^+$ (calc. = 707.115)
Complex 4	
495.045	$[Re^+ + 3CO + HIn + HCOO^- + NH_4^+ + (CH_3CO)]^+$ (calc. = 495.044)
723.118	$[Re^+ + 3CO + AcGluP–2(CH_3CO) + 2H + HIn – H_2O]^+$ (calc. = 723.110)
741.119	$[Re^+ + 3CO + AcGluP–2(CH_3CO) + 2H + HIn]^+$ (calc. = 741.121)
783.130	$[Re^+ + 3CO + AcGluP–CH_3CO + H + HIn]^+$ (calc. = 783.131)
825.142	$[Re^+ + 3CO + AcGluP + HIn]^+$ (calc. = 825.141)

[a] GluQ ($C_{16}H_{18}N_2O_5$); HIn ($C_7H_6N_2$); AcGluP ($C_{20}H_{24}N_2O_9$); acetyl (CH_3CO).

worthy that based on the two anomeric C_1H_β peak integrals (Fig. 8, left), the ratio of the two diastereomers of **4** in D_2O is 0.85, which is similar to the ratio of 0.9 in $CDCl_3$ (Fig. 1, top).

A ^{1}H NMR time study for **3** in D_2O did not show any change over 72 h; however, the spectra were too complex (Fig. S5c) to show the minor release of the indazole ligand into solution, as suggested by its ESI-mass spectrum (Fig. 7, top).

2.3. Cytotoxicity and cellular distribution

Cell viability studies. The cytotoxicity of complexes **1–4** along with cisplatin was measured against a series of cancer cell lines and one primary cell line using the MTT assay after treating the cells with the corresponding compounds for 72 h. The results are shown in Table 3 and Fig. S22–S26. Complexes **1** and **2** were not cytotoxic (IC_{50} > 200 μM), while **3** and **4** showed moderate to low cytotoxicity towards all cell lines. Complex **3** is cytotoxic towards all tested cell lines including the primary cell line (non-cancerous MRC-5) with half-maximal inhibitory concentration (IC_{50}) values in the range of 30–72 μM. Complex **4** is generally less toxic than **3** with IC_{50} = 55–116 μM, except towards the A2780 (ovarian) cancer cells with IC_{50} = 20 ± 5 μM, and shows somewhat lower cytotoxicity towards the primary lung fibroblast cell line MRC-5 (IC_{50} = 96 ± 5). The selectivity index (SI = IC_{50} MRC-5/IC_{50} cancer cell line), calculated from the IC_{50} values, shows that complex **4** is the most selective compound for A2780 ovarian cancer cells (SI = 4.8), while complex **3** exhibits only modest selectivity toward this cell line (SI = 1.8); see Table S12.

The precursor complexes *fac*-[Re(CO)$_3$(*N*,*N*′)Cl] (*N*,*N*′ = GluP and GluQ) were dissolved in water for 48 h and the cell viability of their hydrolyzed products *fac*-[Re(CO)$_3$(*N*,*N*′)(H$_2$O)]$^+$Cl$^-$ was measured; the cationic complex ion did not show any cytotoxicity towards the tested cell lines.

Comparing the IC_{50} trend of **1–4** and their corresponding partition coefficients (log *P*) shows that an increase in log *P* corresponds to a decrease in the IC_{50} value, where complexes **3** and **4** exhibit cytotoxic activity (Table 3). The water/*n*-octanol partition coefficient (log *P*) is a measure of lipophilicity: a higher log *P* is correlated with increased hydrophobicity/lipophilicity of a complex, which is an important property for absorption, distribution, metabolism and excretion of that complex.[52–54] For complexes **1–4**, the log *P* value increases

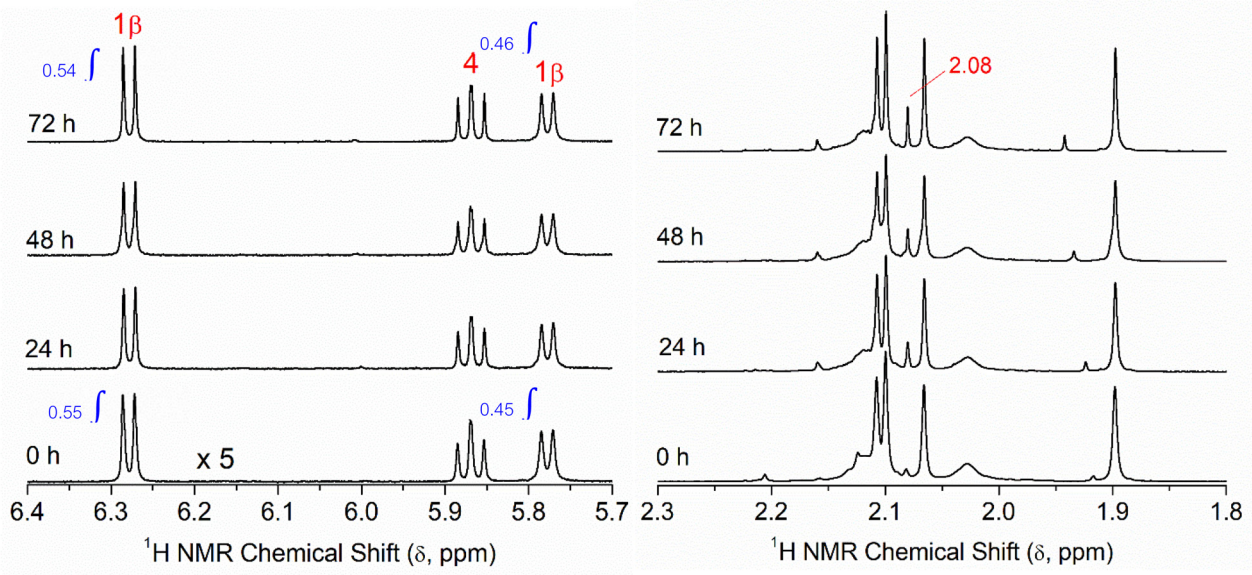

Fig. 8 ^{1}H NMR spectra (600 MHz, 25 °C, D_2O + 10% CD_3OD) of complex **4**, *fac*-[Re(CO)$_3$(AcGluP)(HIn)](OTf), recorded over 72 h, using DSS for internal calibration (δ = 0 ppm); see the full spectrum in Fig. S6c. (Left panel) Anomeric region (scaled × 5) showing two distinct signals for the C_1H_β anomers (1β) with the diastereomeric ratio of 0.85 remaining constant. (Right panel) Acetyl group region showing peaks for CH_3 groups and a small peak at δ = 2.08 ppm (CH_3COO^-) arising from the partial hydrolysis of the acetyl groups.

Table 3 *In vitro* cytotoxicity results (IC_{50} values) at 72 h for complexes **1–4**, hydrolyzed products of their precursors and cisplatin, and their corresponding log *P* values

IC_{50} (μM)						
Complex	A2780	DU-145	MDA-MB-231	A549	MRC-5	log *P*
fac-$[Re(CO)_3(GluP)(H_2O)]Cl$	>200	>200	>200	>200	>200	—
fac-$[Re(CO)_3(GluQ)(H_2O)]Cl$	>200	>200	>200	>200	>200	—
AcGluP	>200	>200	>200	>200	>200	—
1	>200	>200	>200	>200	>200	−1.3 ± 0.3
2	>200	>200	>200	>200	>200	−0.13 ± 0.01
3	29.7 ± 0.6	31 ± 2	36 ± 4	72 ± 2	52 ± 3	0.3 ± 0.1
4	20 ± 5	55 ± 1	92 ± 2	116 ± 4	96 ± 5	0.45 ± 0.03
Cisplatin	8.0 ± 0.5	2.7 ± 0.4	38 ± 4	12 ± 4	14 ± 3	−2.5 ± 0.3[a]

[a] Ref. 3.

from negative (−1.3 ± 0.3 for **1**) to slightly positive values (+0.3 to +0.45 for **3** and **4**, respectively). This is clearly related to their water solubility: while complex **1** is highly soluble in water, **4** dissolves in aqueous solutions containing 0.5–2% methanol or 3–5% acetone, depending on the concentration. Typically, it is expected that the more hydrophobic complexes have higher cell permeability through passive diffusion. However, this does not always increase their cytotoxicity.

One hypothesis drawn from these results was that the more lipophilic complexes **3** and **4** are mainly absorbed by the cells *via* passive diffusion and show cytotoxicity, although the IC_{50} values for **3** are generally lower (more cytotoxic) than those of **4** (more lipophilic), except towards A2780 cells. Cellular uptake measurements of complexes **1** and **2** containing the more hydrophilic GluP ligand could reveal whether these complexes can enter the cells *via* GLUT-mediated transport, despite being non-cytotoxic. The advantage of non-toxic complexes that can accumulate inside cancer cells is that they could have diagnostic applications based on their luminescence properties.[55] However, complexes **1** and **2** did not show any emission upon excitation using their lowest absorption band.

Cellular uptake. One method of measuring the cellular uptake of a metal complex is to digest cells after treatment with the complex and assess the amount of metal content through Inductively Coupled Plasma Mass Spectrometry (ICP-MS) analysis. For this purpose, we chose the HepG2 (liver cancer) cell line that expresses a high number of GLUT-1 protein genes, specifically the SLC2A1 gene with 371 normalized transcripts per million (nTPM).[56] The HepG2 cells were exposed to complex **1** (75 μM) for 72 h (matching the timeline in the cell viability studies), using two different cell culture media: no glucose (NG) and low glucose (LG) levels; see the SI for details. Note that HepG2 cells cannot tolerate high glucose levels. ICP-MS measurements of digested HepG2 cells showed that although the Re uptake was higher in cells grown in no glucose media (Fig. 9), the difference was not statistically significant. Notably, the presence of glucose as the primary GLUT substrate to some extent inhibits the uptake of the glycoconjugated complex **1**. Considering that complex **1** is not lipophilic (log *P* = −1.3 ± 0.3), its cellular uptake in HepG2 cells could be

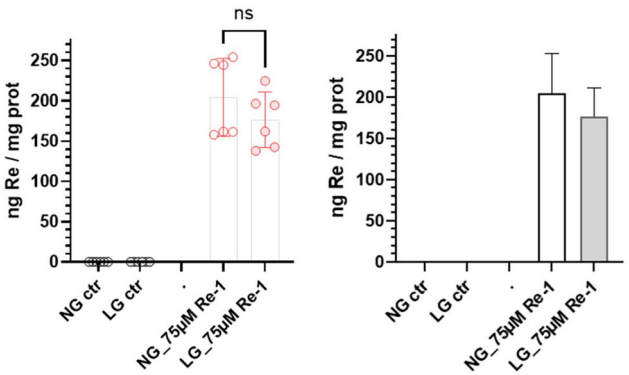

Fig. 9 ICP-MS analysis of the cellular uptake of HepG2 liver cancer cells treated with *fac*-$[Re(CO)_3(GluP)(HIm)](OTf)$ (**1**; 75 μM) for 72 h in no glucose (NG) and low glucose (LG, 1 g L^{-1}) DMEM culture medium. The data bars represent the mean and standard deviation of two biological replicates measured in three technical replicates.

GLUT-mediated. It is noteworthy that complex **1** was not cytotoxic towards HepG2 cells, with IC_{50} = 126 ± 47 and >200 μM in NG media and LG media, respectively.

Cellular localization. Cellular accumulation of complexes **1**, **3** and **4** in A2780 ovarian cancer cells and their elemental distribution maps were obtained using X-ray fluorescence microscopy (XFM), imaging a set of three to four cells in each case (**A–D**) for statistical purposes. XFM was selected as the imaging method since it does not depend on the luminescence properties, such as the fluorescence quantum yield of the Re ions in these complexes, which is a fundamental factor in optical fluorescence microscopy. With this technique, one can detect different elements simultaneously. Since P and Zn have higher concentrations in the nucleus due to DNA structure and zinc-finger proteins,[57] the Zn and/or P distribution maps are used to identify the boundaries of the nucleus, while sulfur mainly accumulates in the cytosol as glutathione.[58] Therefore, obtaining the elemental distribution maps for biologically important elements such as Zn, Fe, Cu, Ca, S, and P, as well as that of Re, helps us understand the rhenium accumulation in different organelles through co-localization.

Since the fluorescence of Re $L_{\alpha1}$ (8652.5 eV) and Zn $K_{\alpha1}$ (8638.9 eV) overlapped, the Re $L_{\beta1}$ emission line (10 010.0 eV) was used to obtain its elemental distribution in the cells.

Fig. 10 and Fig. S27–S30 show the elemental distribution maps in A2780 cells after being treated for 6 h with 20 μM solutions of **1**, **3**, and **4** in DMEM (5% acetone in DMEM for **4**), or only with DMEM (control cells). Comparing all these images shows that cells treated with complex **3** display the strongest Re signal, which accumulates in the same region as Zn, indicating that the main cellular target for complex **3** is the nuclear/perinuclear area. Localization of Re in nuclear and perinuclear regions was previously observed in MDA-MB-231 cells that were

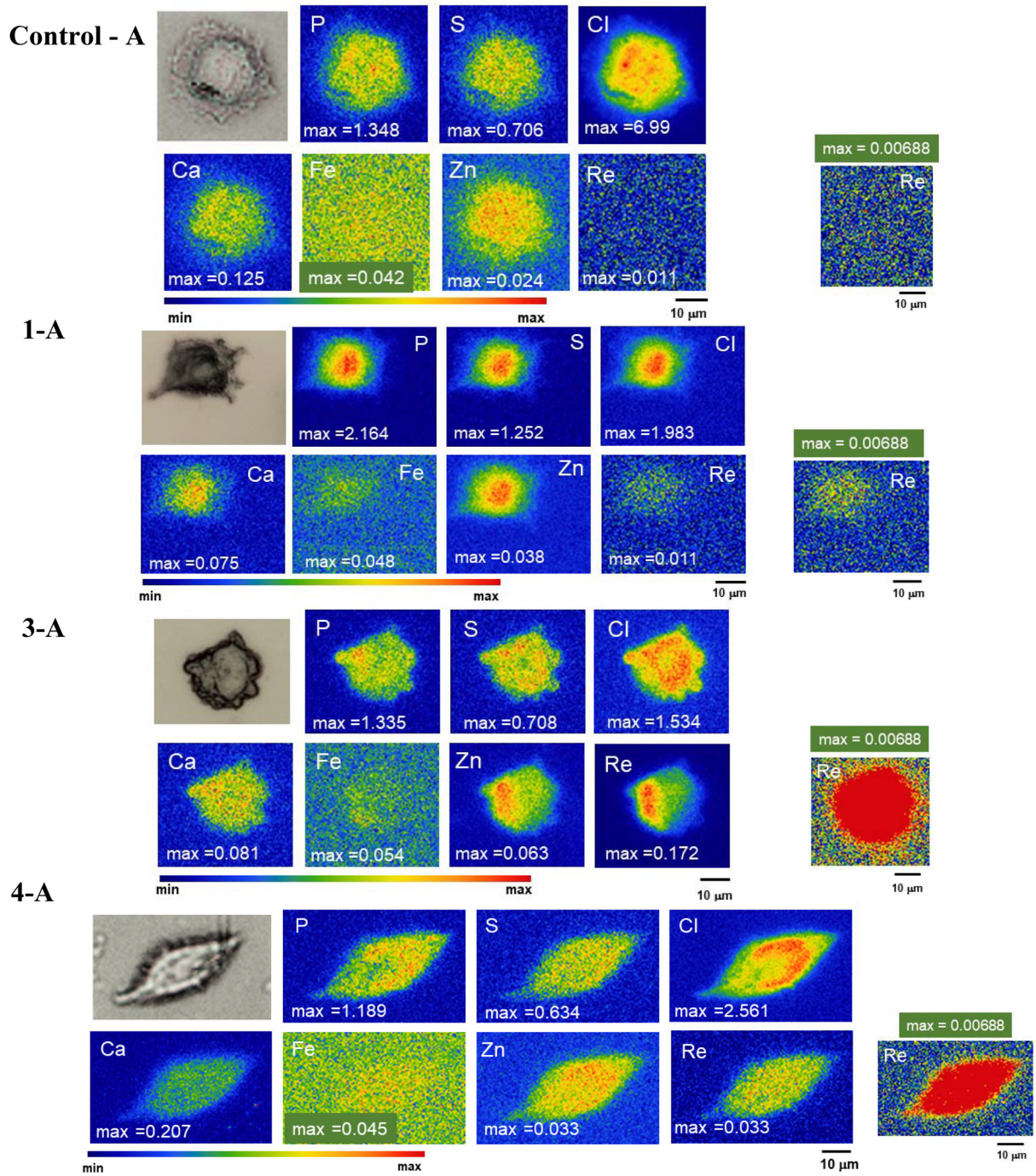

Fig. 10 Optical micrographs (top left panel) and XFM elemental distribution map of the A2780 control cells in DMEM and those treated for 6 h with 20 μM of complexes *fac*-[Re(CO)$_3$(GluP)(HIm)]OTf (**1**), *fac*-[Re(CO)$_3$(GluQ)(HIn)]OTf (**3**) in DMEM, and *fac*-[Re(CO)$_3$(AcGluP)(HIn)]OTf (**4**) in (DMEM + 5% acetone). The maximum elemental area densities (μg cm^{-2}) obtained from standards are given at the bottom of each map, where spots with the highest area density are shown in red.

exposed to *fac*-[Re(CO)$_3$(bpy)(H$_2$O)](OTf).[59] Co-localization of Re with P and Zn was also observed for HeLa cells treated with the *fac*-[Re(CO)$_3$(dmphen)(*p*-tolylisonitrile)](OTf) complex.[31]

The maximum elemental area densities were measured in the four imaged cells treated with this complex (**3-A** through **3-D** in Fig. 10 and Fig. S29) and show that for Re the mean is 0.196 ± 0.101 μg cm^{-2} (± standard deviation). The cells treated with complex **4** show a significantly lower Re signal, which, like Zn, has a rather uniform distribution across the cell. Indeed, for the three imaged cells treated with complex **4** (cells **4-A** through **4-C** in Fig. 10 and Fig. S30), it was not possible to easily locate the nuclear position, *i.e.* areas with higher Zn and/or P density. In these cells, the average maximum area density for Re is 0.034 ± 0.005 μg cm^{-2}, which is about 17% of that of complex **3**. If passive diffusion was the only pathway for cellular uptake of these cationic complexes, higher Re area density values would be expected for **4** that has higher lipophilicity than **3**, with log *P* values of 0.45 ± 0.03 and 0.3 ± 0.1, respectively (Table 3). Moreover, dissolution of complex **4** in aqueous or cell culture media requires a small percentage of organic solvents, such as methanol (0.5–2%) or acetone (3–5%), depending on the desired concentration in solution. Therefore, the higher Re accumulation in cells treated with the water-soluble complex **3** (relative to **4**) could indicate partial GLUT-mediated transport of this complex. Note that for complex **4** this mode of transport is inhibited due to the sugar –OH protection.

A closer look at the images obtained for the control cells in Fig. 10 and Fig. S27 (control-**A** to control **C**) reveals that there is a small signal in the Re distribution map that would correspond to a fictional average maximum area density of 0.010 ± 0.001 μg cm^{-2}, even though the control cells were only treated with DMEM. This signal is due to the presence of trace contaminants like tungsten and gallium in the beamline. Tungsten emission lines, $L_{\beta1}$ = 9672.4 eV and $L_{\beta2}$ = 9961.5 eV, almost overlap with the Re $L_{\beta1}$ line at 10 010.0 eV. Also, gallium emission ($K_{\beta1}$ = 10 264.2 eV) makes the fitting of the nearby Re signal in the XFM spectrum rather difficult. It also interferes with the less intense Re $L_{\beta2}$ line at 10 275.2 eV.

The presence of such a background signal in the Re distribution maps makes it challenging to detect trace amounts of

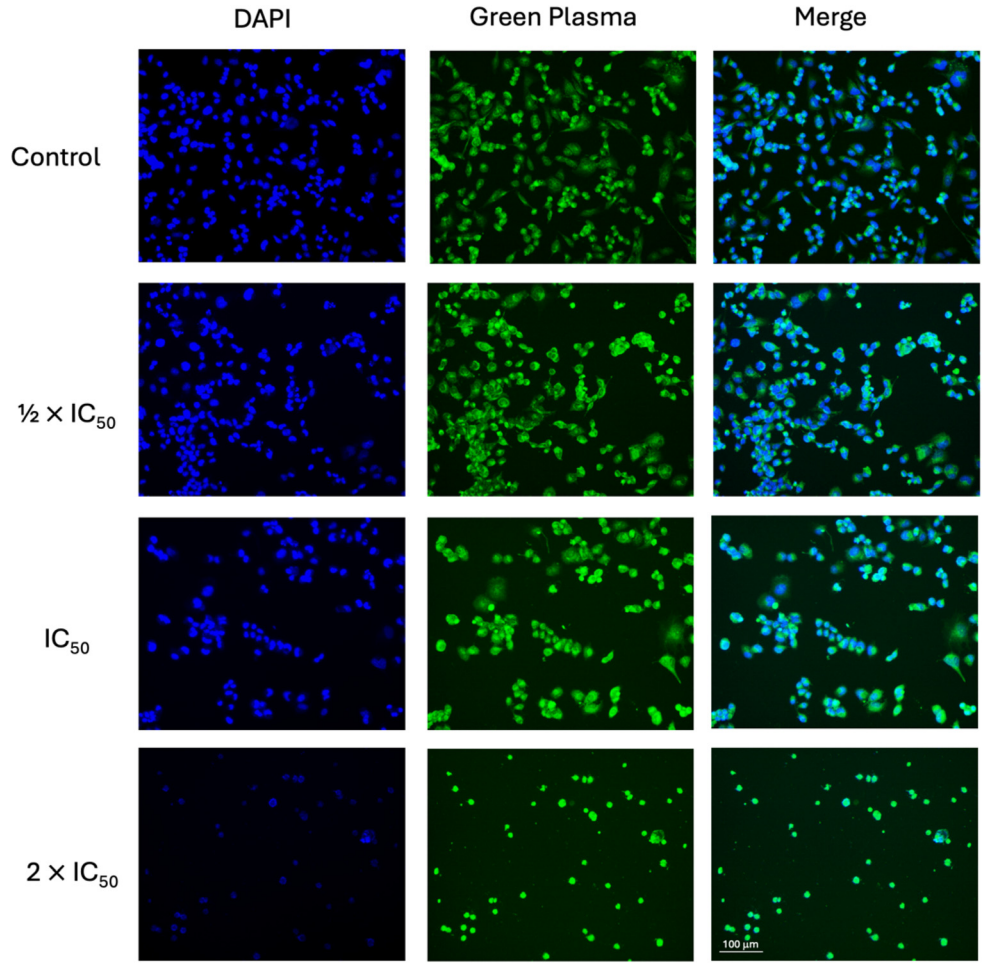

Fig. 11 Changes in the morphology of A2780 ovarian cancer cells observed in fluorescence microscopy images with Green Plasma and DAPI markers. The images were obtained after treatment of cells with complex **4** for 72 h at concentrations of $\frac{1}{2}$ × IC$_{50}$ (10 μM), IC$_{50}$ (20 μM), and 2 × IC$_{50}$ (40 μM). The negative control was treated with DMEM + 5% acetone. The images were captured using a CELENA microscope at 10× magnification.

Re in the cells. For example, in the XFM spectra of cells treated with complex **1**, a small Re $L_{\beta 1}$ peak is observed (Fig. S31 and S32). Fitting this Re peak in the XFM spectra of the four cells treated with complex **1** resulted in Re distribution maps (**1-A** through **1-D**) having an average maximum area density of 0.018 ± 0.012 μg cm^{-2}, which is slightly higher than that in the control cells (0.010 ± 0.001 μg cm^{-2}), but not statistically significant (p-value = 0.328). This means that we cannot detect any clear Re signal within the cell boundary, as the detected emission in the Re region for these cells is the sum of emission from the traces of Re in complex **1** taken up by the cells, and the emissions from tungsten/gallium contaminants in the beamline, which artificially increase the Re maximum density (as seen for the control cells). The contrast images of the Re distribution in the cell treated with complex **1** (**1-A**) *vs.* the control cell (control-**A**) are displayed in Fig. 10, right panel.

It is noteworthy that despite the weak Re signal detected by XFM in A2780 ovarian cells treated for 6 h with a 20 μM solution of complex **1**, the ICP-MS data showed that HepG2 liver cells with a high number of GLUT-1 protein genes, when treated for a longer period (72 h) with a more concentrated (75 μM) solution of **1**, exhibited a significant uptake of this complex (Fig. 9).

The contrast images on the far-right compare the detected Re signal when lowering the maximum area density to 0.00688 μg cm^{-2} for this energy region for all samples. The threshold for the maximum area density has been intentionally lowered in these images to be able to detect the Re signal in the **1-A** cell. In cells **3-A** and **4-A** that have significantly higher Re content than this artificial maximum threshold, all spots appear in red color.

Cellular morphology. Monitoring cell morphology after exposure to a cytotoxic complex can hint towards a possible mechanism of action; for details of the methodology, see the SI. For this purpose, A2780 cells were treated with complex **4**, the most cytotoxic complex towards this cell line, at 5 μM, 10 μM, 20 μM (IC_{50} concentration), and 40 μM before introducing any dye. It was initially observed that the cell density significantly decreased over 72 h. DAPI and Green Plasma dyes mark the adenine–thymine regions in the nucleus and the cell plasma membrane, respectively.[60] After 72 h, the cells exposed to **4** at the IC_{50} concentration and higher experience a loss of nuclear integrity along with cytoplasmic shrinkage, which is often indicative of apoptosis[61] (Fig. 11 and Fig. S33). The clonogenic assay further concluded that complex **4** mainly acts as a cytotoxic rather than cytostatic agent, as it largely kills the cells in the colonies rather than inhibiting their growth (Fig. S34).

3. Conclusions

This study outlines the syntheses and structural characterization of four Re(I) glycoconjugated complexes as their triflate salts with the general formula *fac*-[Re(CO)$_3$(*N*,*N*′)L](OTf), where (*N*,*N*′) = GluP, GluQ, or AcGluP and L = imidazole or indazole, and also reports their *in vitro* cytotoxicity against a series of cancer cell lines and a primary cell line. Complexes **1** and **2** are highly soluble in water, while complex **3** has limited water solubility (~1 mM) and complex **4** dissolves in aqueous solutions containing 0.5–2% methanol or 3–5% acetone, depending on the concentration. These complexes were relatively stable in aqueous solution over 72 h, as monitored by UV-vis and ESI-MS time studies: for complex **3**, the dissociation of the axial indazole ligand occurred only for a small fraction, while for complex **4** only trace amounts of loss of the glycoconjugated AcGluP ligand or partial de-acetylation of AcGluP was observed over time. Complexes **3** and **4** having higher log P values (0.3–0.45) showed moderate cytotoxicity against several cancer cell lines, especially the A2780 ovarian cancer cells. XFM images revealed that A2780 cells treated with **3** exhibited the highest cellular Re accumulation, primarily within the nuclear/perinuclear region, co-localized with Zn-rich areas. In contrast, **4** showed a lower and more broadly distributed intracellular Re signal. Because of its acetylated glucose moiety and higher lipophilicity, complex **4** was considered to be a useful comparison, as pathways for its uptake would not depend on direct glucose recognition. However, the current cellular accumulation results for **4** could be slightly affected by a small amount of hydrolysis of its AcGluP acetylated groups, although the ESI-MS data (Fig. S8c) show this to be insignificant during the 6 h drug exposure time used in the XFM experiments. These findings indicate that glucose transport pathways may be partially involved in the uptake of complex **3**; however, additional mechanistic studies are needed to confirm this hypothesis. XFM images showed minimal accumulation of complex **1** in A2780 cells. Meanwhile ICP-MS analysis of HepG2 cells treated with this complex revealed a trend towards higher uptake under glucose-free conditions. These results provide preliminary support for the involvement of glucose transport pathways. To the best of our knowledge, complexes **1** and **3** are the first water soluble, stable glycoconjugated Re(CO)$_3^+$ complexes with a direct bond to a glucose-derived entity that may be at least partially transported by the GLUTs. We will continue to explore the cytotoxicity of other stable glycoconjugated complexes with GLUT-mediated transport, by changing the ligands, metal ions and their coordination geometry.

4. Experimental section

4.1. Materials and reagents

Chemical reagents Re(CO)$_5$Cl (Sterm Chemicals), D-glucosamine hydrochloride, 1*H*-indazole (HIn), 2-quinoline carboxaldehyde (Fischer Scientific), 1,3,4,6-tetra-*O*-acetyl-β-D-glucosamine hydrochloride (Thermo Scientific), 2-pyridine carboxaldehyde, silver trifluoromethanesulfonate, imidazole (HIm), triethylamine, absolute ethanol, diethyl ether, dichloromethane (Sigma-Aldrich), and sodium hydroxide (Merck) were purchased and used without further purification. Tetrahydrofuran (THF, Sigma-Aldrich) was distilled over type 4A molecular sieves to remove the butylated hydroxytoluene

(BHT) stabilizer, which would otherwise give intense peaks in the NMR spectra. Sephadex LH-20 (Sigma-Aldrich) was soaked in methanol or ethanol for 24 h before packing the column.

Cell culture. The cancer cell lines DU-145 (prostate), MDA-MB-231 (breast), and A549 (lung), and the primary cell line MRC-5 (lung) were acquired from Sigma-Aldrich and cultured in low glucose (1 g L^{-1}) DMEM (Dulbecco's modified Eagle's medium) supplemented with 10% fetal bovine serum (FBS), penicillin (100 units per mL), gentamicin (50 mg L^{-1}), and amphotericin (25 μg mL^{-1}). The A2780 (ovarian) cancer cell line (Sigma-Aldrich) was similarly cultured in RPMI 1640 medium (Roswell Park Memorial Institute) with the same supplements. 10× PBS (phosphate-buffered saline) was diluted 10-fold with Milli-Q water to obtain 1× PBS. Dulbecco's PBS (D-PBS) and 1× PBS solutions were sterilized by passing through a Nalgene filter before use. All cell lines were maintained in culture flasks in a humidified 5% CO_2 incubator at 37 °C.

4.2. Syntheses and characterization

2-Deoxy-2-[(2-quinolinylmethylene)amino]-D-glucose (GluQ). This compound was prepared with a slight modification of a previously reported procedure (see the SI).[42]

1,3,4,6-Tetra-*O*-acetyl-2-deoxy-2-β-[(2-pyridinylmethylene) amino]-D-glucose (AcGluP). This compound was also synthesized by modifying a previously described method in the literature (see the SI).[43]

***fac*-[Re(CO)$_3$(GluP)Cl].** This precursor compound was synthesized and characterized as described elsewhere.[28]

fac-[Re(CO)$_3$(GluP)(HIm)](CF$_3$SO$_3$) (1). Silver trifluoromethanesulfonate, $Ag(CF_3SO_3)$ (0.20 mmol), was added to *fac*-[Re$(CO)_3$(GluP)Cl] (0.17 mmol) in ~20 mL of acetone and refluxed at 56 °C for 3 h under an argon atmosphere in darkness to form *fac*-[Re$(CO)_3$(GluP)(CF_3SO_3)]. The silver chloride precipitate was filtered, and imidazole (HIm, 0.20 mmol) was added and stirred overnight at room temperature (RT) under argon. After removing the solvent, the mixture was passed through a Sephadex LH-20 size exclusion chromatography column with absolute ethanol as the mobile phase, to separate the unreacted reagents. The main orange band was collected and evaporated to dryness using a rotary evaporator, and the product was washed with diethyl ether and dried under vacuum. Yield 54%. Elemental anal. calcd for [Re$(CO)_3(C_{12}H_{16}N_2O_5)(C_3H_4N_2)$]$(CF_3SO_3)$ ($ReC_{19}H_{20}N_4O_{11}SF_3$): %C 30.20, %H 2.67, %N 7.41, %S 4.24; found %C 30.31, %H 2.72, %N 7.65, %S 4.32. ^{1}H NMR (600 MHz, 25 °C, CD_3OD; the chemical shift range covers signals for a specific H in all four diastereomers) δ_H 9.23–9.42 (s, 1H, C_7H), 9.08–9.18 (d, J = 6 Hz, 1H, $C_{12}H$), 8.34–8.38 (m, 1H, $C_{10}H$), 8.26–8.32 (m, 1H, C_9H), 7.82–7.85 (m, 1H, $C_{11}H$), 7.68–7.82 (s, 1H, $C_{13}H$), 7.04–7.13 (m, 1H, $C_{14}H$), 6.72–6.89 (m, 1H, $C_{15}H$), 5.74 (d, J = 3 Hz, 0.1H, $C_1H\alpha$), 5.43 (d, J = 6 Hz, 0.4H, $C_1H\beta$), 5.09 (d, J = 6 Hz, 0.3H, $C_1H\beta$), 5.04 (d, J = 3 Hz, 0.1H, $C_1H\alpha$), 4.39–4.43 (m, 0.3H, $C_5H\alpha$), 4.36–4.37 (m, 0.2H, $C_4H\alpha$), 4.17–4.20 (m, 0.3H, $C_3H\alpha$), 3.92–3.94 (m, 1H, C_6H, two diastereotopic H), 3.83–3.86 (m, 0.7H, $C_3H\beta$), 3.71–3.75 (m, 0.9H, C_6H), 3.59–3.62 (m, 1H, C_2H), 3.42–3.52 (m, 1.7H, $C_4H\beta$, $C_5H\beta$). ^{13}C NMR (151 MHz, CD_3OD) δ_C 198.1 (CO_{eq}), 196.5 (CO_{eq}), 190.7 (CO_{ax}), 172.4–175.0 (C_7), 155.7–156.6 (C_8), 154.9–155.0 (C_{12}), 142.5–142.8 (C_{10}), 140.2–140.4 (C_{13}), 131.7–131.9 (C_{11}), 131.4–131.5 (C_{15}), 131.5–131.7 (C_9), 119.5–119.6 (C_{14}), 96.4–97.0 ($C_1\beta$), 92.0–92.1 ($C_1\alpha$), 82.3–82.4 (C_2), 77.8–78.5 (C_4), 75.4–75.6 (C_3), 70.2–73.6 (C_3, C_5), 62.6–62.7 (C_6). MS (ESI, positive mode): +*m*/*z* (relative intensity) 579.090 ([**1** – CO–$CF_3SO_3^-$]$^+$, 15), 607.096 ([**1** – $CF_3SO_3^-$]$^+$, 100). IR (ATR, cm^{-1}): $\nu_{C=O}$ = 2025, 1889; ν_{C-OH} = 1025 cm^{-1}. Water/*n*-octanol partition coefficient (log *P*) = −1.3 (± 0.3).

fac-[Re(CO)$_3$(GluP)(HIn)](CF$_3$SO$_3$) (2). This compound containing complex **2** was prepared using 1*H*-indazole (Re : HIn = 1 : 1 mole ratio) following a similar procedure to that used for **1** and was purified using a Sephadex LH-20 column with distilled THF as the mobile phase, affording the main bright orange band. After removing the solvent, the solid residue was washed with diethyl ether and dried under vacuum. Yield 80%. Elemental anal calcd for $[Re(CO)_3(C_{12}H_{16}N_2O_5)(C_7H_6N_2)](CF_3SO_3)\ [(C_2H_5)_2O]$ ($ReC_{27}H_{32}N_4O_{12}SF_3$): %C 36.86, %H 3.67, %N 6.37, %S 3.64; found %C 36.73, %H 3.32, %N 7.49, %S 3.43. ^{1}H NMR (600 MHz, 25 °C, CD_3OD; the chemical shift range covers signals for a specific H in all four diastereomers) δ_H 9.37–9.47 (s, 1H, C_7H), 9.14–9.23 (d, J = 6 Hz, 1H, $C_{12}H$), 8.28–8.38 (m, 2H, $C_{10}H$, C_9H), 8.03–8.18 (s, 1H, $C_{21}H$), 7.82–7.86 (m, 1H, $C_{11}H$), 7.64–7.77 (m, 1H, $C_{23}H$), 7.37–7.54 (m, 2H, $C_{25}H$, $C_{26}H$), 7.13–7.22 (m, 1H, $C_{24}H$), 5.66 (d, J = 3 Hz, 0.1H, $C_1H\alpha$), 5.39 (d, J = 6 Hz, 0.5H, $C_1H\beta$), 5.13 (d, J = 6 Hz, 0.2H, $C_1H\beta$), 5.06 (d, J = 3 Hz, 0.1H, $C_1H\alpha$), 4.30–4.62 (m, 1H, C_3H), 4.01–4.19 (t, 1H, C_4H), 3.71–3.95 (m, 3H, C_2H + C_6H with two diastereotopic H), 3.51–3.65 (m, 1H, C_5H). ^{13}C NMR (151 MHz, CD_3OD) δ_C 196.9 (CO_{eq}), 195.3 (CO_{eq}), 190.2 (CO_{ax}), 173. 9–176.5 (C_7), 156.4 (C_8), 155.1 (C_{12}), 142.8 (C_9) 139.7 (C_{21}), 138.2 (C_{27}), 134.8 (C_{22}), 132 (C_{11}), 131.5 (C_{10}), 130.7 (C_{26}), 123.8 (C_{25}), 122.0 (C_{23}), 111.1 (C_{24}), 91.7–96.5 (C_1), 82.1 (C_2), 78.4 (C_3, one diastereomer), 78.0 (C_5, one diastereomer), 73.5–78.9 (C_4), 71.9 (C_5, one diastereomer), 71.2 (C_3, one diastereomer), 62.4 (C_6). MS (ESI, positive mode): +*m*/*z* (relative intensity) 657.100 ([**2** – $CF_3SO_3^-$]$^+$, 100). $\nu_{C=O}$ = 2031, 1912; ν_{C-OH} = 1027 cm^{-1}. Water/*n*-octanol partition coefficient (log *P*) = −0.13 (± 0.01).

fac-[Re(CO)$_3$(GluQ)(HIn)](CF$_3$SO$_3$) (3). The precursor compound, *fac*-[Re$(CO)_3$(GluQ)Cl], was prepared by refluxing Re$(CO)_5$Cl (0.55 mmol) in ~15 mL of absolute ethanol at 68 °C for 6 h under argon. The solution was cooled down to RT and a suspension of GluQ (0.55 mmol) in 50 mL of absolute ethanol was added and stirred for 2 h under argon at RT. After reducing the volume, the mixture was passed through two consecutive Sephadex LH-20 columns with ethanol as the mobile phase, affording the main dark red band. Upon addition of diethyl ether to the separated main band, a red *fac*-[Re$(CO)_3$(GluQ)Cl] powder formed.

$Ag(CF_3SO_3)$ (0.11 mmol) was added to *fac*-[Re$(CO)_3$(GluQ)Cl] (0.09 mmol) in ~20 mL of acetone and refluxed for 3 h under an argon atmosphere in darkness. After filtering the silver chloride precipitate, 1*H*-indazole (0.11 mmol) was added and

the solution was stirred overnight at RT under argon. After reducing its volume, the mixture was passed through a Sephadex LH-20 column with distilled THF as the mobile phase. The main orange band was isolated and washed with diethyl ether and dried under vacuum. Yield 56%. Elemental anal. calcd for $[Re(CO)_3(C_{16}H_{18}N_2O_5)(C_7H_6N_2)](CF_3SO_3)[(C_2H_5)_2O]_{0.75}$ ($ReC_{30}H_{31.5}N_4O_{11.75}SF_3$): %C 39.54, %H 3.48, %N 6.15, %S 3.52; found %C 39.91, %H 3.56, %N 6.98, %S 2.89. ^{1}H NMR (600 MHz, 25 °C, CD_3OD; the chemical shift range covers signals for a specific H in all four diastereomers) δ_H 9.62–9.74 (s, 1H, C_7H), 8.72–8.98 (m, 2H, C_9H + $C_{13}H$), 8.12–8.34 (m, 3H, $C_{10}H$ + $C_{14}H$ + $C_{16}H$), 7.70–8.05 (m, 2H, $C_{15}H$ + $C_{21}H$), 7.36–7.58 (m, 3H, $C_{23}H$ + $C_{25}H$ + $C_{26}H$), 7.11–7.16 (m, 1H, $C_{24}H$), 5.70–5.72 (d, J = 3 Hz, 0.5H, $C_1H\alpha$), 5.50 (d, J = 6 Hz, 0.5H, $C_1H\beta$), 4.49–4.80 (m, 1H, C_3H), 3.75–4.01 (m, 3H, C_4H + C_6H with two diastereotopic H), 3.58–3.70 (m, 2H, C_2H + C_5H). ^{13}C NMR (151 MHz, $CDCl_3$, the most intense peaks from the species are assigned) δ_C 196.7 (CO_{eq}), 194.6 (CO_{eq}), 189.9 (CO_{ax}), 175.7 (C_7), 149.1 (C_8), 144.4 (C_9), 142.7 (C_{12}), 140.0 (C_{27}), 135.1 (C_{10}), 133.9 (C_{11}), 129.7 (C_{13}), 130.8 (C_{14}), 131.1 (C_{25}), 131.9–132.1 (C_{15} + C_{21}), 127.8 (C_{22}), 125.6 (C_{16}), 123.8 (C_{24}), 123.9 (C_{23}), 111.1 (C_{26}), 96.4 ($C_1\beta$), 91.7 ($C_1\alpha$), 78.4 (C_2), 73.6 (C_4), 72.1 (C_5), 71.2 (C_3), 62.5 (C_6). MS (ESI, positive mode): $+m/z$ (relative intensity) 707.114 ($[\mathbf{4} - CF_3SO_3^-]^+$, 100). $\nu_{C=O}$ = 2033, 1910; ν_{C-OH} = 1027 cm^{-1}. Water/*n*-octanol partition coefficient (log *P*) = +0.13 (± 0.1).

*fac-[Re(CO)$_3$(β-AcGluP)(HIn)](CF$_3$SO$_3$) (**4**).* The precursor compound, *fac*-[$Re(CO)_3$(AcGluP)Cl], was prepared by refluxing $Re(CO)_5Cl$ (0.26 mmol) in ~15 mL of absolute ethanol for 6 h at 68 °C under an argon atmosphere. After removing the solvent, ~15 mL of acetone was added to the remaining yellow oil and stirred at RT under an argon atmosphere overnight, to exchange the coordinated ethanol in $Re(CO)_3(EtOH)_2Cl$ with acetone, which would then allow for easy ligand substitution in the next step. The solvent was removed using a rotary evaporator, and to the remaining, AcGluP dissolved in 15 mL of dichloromethane (0.26 mmol) was added and stirred overnight under argon at RT. After reducing the volume, the mixture was passed through two consecutive Sephadex LH-20 columns with distilled THF as the mobile phase. Upon addition of pentane to the separated main band, a dark orange powder *fac*-[$Re(CO)_3$(AcGluP)Cl] was formed. Mixing this compound (0.13 mmol) with $Ag(CF_3SO_3)$ (0.16 mmol) in dichloromethane for 3 days under argon in the dark led to the formation of the solid compound *fac*-[$Re(CO)_3$(AcGluP)(CF_3SO_3)].

To the above triflate salt (0.08 mmol) dissolved in 10 mL of dichloromethane, 1.2 equivalents of 1*H*-indazole (0.11 mmol) were added and stirred for 48 h at RT under argon. After removing the solvent, the mixture was passed through a Sephadex LH-20 column with methanol as the mobile phase. The product was dried under vacuum. Yield 74%. Elemental anal. calcd for $[Re(CO)_3(C_{20}H_{24}N_2O_9)(C_7H_6N_2)](CF_3SO_3)$ ($ReC_{31}H_{30}N_4O_{15}SF_3$): %C 38.23, %H 3.10, %N 5.75, %S 3.29; found %C 38.33, %H 3.34, %N 5.56, %S 3.13. ^{1}H NMR (600 MHz, 25 °C, $CDCl_3$; the chemical shift range covers signals for a specific H in both diastereomers) δ_H 11.22–11.38 (s, 1H, NH), 9.45–9.58 (s, 1H, C_7H), 9.79–9.85 (d, J = 6 Hz, 1H, $C_{12}H$), 8.68–8.77 (d, J = 6 Hz, 1H, C_9H), 8.38–8.39 (m, 1H, $C_{10}H$), 8.33–8.37 (m, 1H, $C_{11}H$), 7.68–7.75 (m, 2H, $C_{21}H$ & $C_{23}H$), 7.56–7.62 (m, 1H, $C_{26}H$), 7.40–7.44 (m, 1H, $C_{25}H$), 7.20–7.25 (m, 1H, $C_{24}H$), 6.15 (d, J = 6 Hz, 0.5H, $C_1H\beta$), 5.99 (d, J = 6 Hz, 0.5H, $C_1H\beta$), 5.63–5.70 (m, 1H, C_4H), 5.09–5.20 (m, 1H, C_3H), 4.31–4.38 (m, 1H, C_2H), 4.07–4.38 (m, 2H, C_6H two diastereotopic H), 3.99–4.06 (m, 1H, C_5H), 1.87–2.10 (s, 12H, $C_{14}H$, $C_{16}H$, $C_{18}H$, $C_{20}H$). ^{13}C NMR (151 MHz, 25 °C, $CDCl_3$) δ_C 194.8–194.9 (CO_{eq}), 193.7–194.0 (CO_{eq}), 187.6–188.4 (CO_{ax}), 177.1–177.6 (C_7), 169.3–170.6 (CO: C_{13} + C_{15} + C_{17} + C_{19}), 167.8–168.2 (C_{27}), 154.4–154.5 (C_8), 153.0–153.2 (C_{12}), 141.9–142.2 (C_{10} + C_{11}), 133.4–133.5 (C_9), 131.1 (C_{21}), 130.1–130.2 (C_{25}), 123.5–123.7 (C_{24}), 122.8 (C_{22}), 120.5 (C_{23}), 111.8–112.0 (C_{26}), 92.0–93.0 (C_1), 75.3–75.5 (C_2), 72.8–73.2 (C_5), 72.2–72.4 (C_4), 68.8–69.1 (C_3), 61.4 (C_6), 19.9–20.8 (C_{14} + C_{16} + C_{18} + C_{20}). MS (ESI, positive mode): $+m/z$ (relative intensity) 825.142 ($[\mathbf{6} - CF_3SO_3^-]^+$, 100). $\nu_{C=O}$ = 2024, 1888; $\nu_{C=O}$ (acetyl) = 1746; ν_{C-O} (ester) = 1202; ν_{C-OH} = 1033 cm^{-1}. Water/*n*-octanol partition coefficient (log *P*) = +0.45 (± 0.03).

4.3. Physical measurements

ESI-mass spectrometry. High-resolution electrospray ionization (ESI) mass spectra were recorded in both positive (+) and negative (–) ion modes using an Agilent 6520 Q-TOF instrument. Freshly dissolved dilute solutions of solid compounds **1–3** in water and **4** in 0.5% methanol aqueous solution were injected and mobilized at an injection flow rate of 0.2 mL min^{-1} and a drying gas flow rate of 7 L min^{-1} at 200 °C. Capillary, skimmer, and fragmentor voltages were set at 4000, 65, and 80 V, respectively. Peak assignments were confirmed in the high-resolution mode using an Isotope Distribution Calculator from Scientific Instrument Services.[62] The ESI-mass spectrum of each solution was recorded after 72 h to check the stability of the complex ions.

Infrared spectroscopy. FT-IR spectra of the solid salts of complexes **1–4** were recorded using an Agilent Cary 630 FT-IR spectrometer equipped with an attenuated total reflectance (ATR) accessory. For each sample, 32 scans with a spectral resolution of 4 cm^{-1} were averaged.

NMR spectroscopy. ^{1}H- and ^{13}C-NMR spectra were recorded at room temperature with a Bruker 600 MHz Avance III spectrometer using CD_3OD (for **1–3**) or $CDCl_3$ (for **4**) as the solvent. For each ^{1}H NMR spectrum, a total of 128 scans were co-added and the solvent residual signal (at 3.31 ppm for CHD_2OD and 7.26 ppm for $CHCl_3$) was used for internal calibration.[48] The ^{13}C NMR spectra were recorded using broadband proton decoupling at 151 MHz, a 30° pulse, a 26.2 kHz sweep width, 65 K data points and the uniform driven equilibrium Fourier transform (uDEFT) pulse sequence[63] with a 4s delay between scans, which allowed observing the quaternary CO (carbonyl) carbons that lack a proton and have long relaxation times. A total of 12 000 scans were collected overnight and calibrated by internally referencing to the solvent signal (at 49.15 ppm for CHD_2OD and at 77.2 ppm for $CDCl_3$).[64] 2D NMR spectra, *i.e.* Heteronuclear Single Quantum Coherence Spectroscopy

(HSQC) were recorded using a Bruker Avance III spectrometer operating at 600 MHz (for **1**) and 400 MHz (for **2–4**), with 8–12 scans collected for each.

The ^{1}H NMR time studies were carried out for complexes **3** (1 mM in D_2O) and **4** (6 mM in D_2O + 10% CD_3OD), using sodium 4,4-dimethyl-4-silapentane-1-sulfonate (DSS) for internal calibration (δ = 0 ppm). All spectra of **3** were normalized relative to the DSS peak integral.

UV-vis spectroscopy. Electronic absorption spectra were recorded using a Cary 300 UV-vis spectrophotometer. Samples for time studies were freshly prepared (50 μM) in water (for **1–3**) or in 0.5% methanol aqueous solution (for **4**) at room temperature and placed in a 1.0 cm quartz cell, using the solvent as a blank. The measurements were repeated after 72 h to monitor their stability over time.

X-ray absorption spectroscopy (XAS). Re L_3-edge X-ray absorption spectra of the solid compounds **1–3** were recorded at room temperature in both transmission and fluorescence modes simultaneously by placing the sample at 45° relative to the beam and using a Passivated Implanted Planar Silicon (PIPS) fluorescence detector at the BioXAS-Main beamline of the Canadian Light Source (CLS, 2.9 GeV and 220 mA). Higher harmonics were removed by detuning the Si (220) double-crystal monochromator to 60% of the maximum beam intensity at 10 600 eV. The spectrum of **4** in the solid state was recorded in transmission mode at room temperature at beamline 12C at the Photon Factory, High Energy Accelerator Research Organization, Japan (PF - KEK, 2.5 GeV, 450 mA), equipped with a Si(111) monochromator crystal and Rh-coated higher harmonic rejection mirror. The ion chambers (I_0 and I_1) were filled with N_2 gas. Rhenium foil was used for external calibration of incident beam energy, setting its first inflection point at 10 535 eV. The solid samples were finely ground and mixed with boron nitride at a BN : sample ratio of 40 : 60 (w/w) and packed into a 1 mm aluminum frame with Mylar tape as the window. For each sample three to four scans were collected and compared before averaging using the Athena program[65] to check for potential beam damage.

Extended X-ray absorption fine structure (EXAFS) oscillations were extracted using the WinXAS 3.1 program,[66] and processed as described elsewhere[28] with the threshold energy E_0 varying between 10 539.4 eV (**4**) and 10 540.5–10 541.2 eV (**1–3**). Structural data from the standard compound *fac*-[Re$(CO)_3$(bpy)(H_2O)](OTf)[29] (OTf^- = $CF_3SO_3^-$) were used for the ATOMS program,[67] which generated the input file for the FEFF 7.02 program,[68,69] for simulating EXAFS oscillations.

Least-squares curve fitting of the simulated EXAFS model functions to the experimental EXAFS spectra was carried out over a k-range of 2.4–15.9 Å^{-1}, fixing the coordination number, N_i, while refining the bond distance (R_i) and the Debye–Waller parameter (σ^2), allowing ΔE_0 to float as a common value for all paths. The amplitude reduction factor ($S_0{}^2$) was initially refined for all EXAFS spectra, which led to lower values for the fluorescence data ($S_0{}^2$ ~0.8) shown in Fig. S10, compared to the transmission data ($S_0{}^2$ ~1.1) presented in Fig. 3. To ensure that the EXAFS refinement results including the Debye–Waller parameter (σ^2) values in Table 1 are comparable for the solid compounds of **1–4**, the $S_0{}^2$ value was fixed at 1.0 for all fittings shown in Fig. 3. The accuracy of the average bond distances is within ± 0.02 Å, and the estimated error limit for the Debye–Waller parameters is ± 0.001 Å^2.

X-ray fluorescence microscopy (XFM). Silicon nitride windows (1.5 mm × 1.5 mm × 500 nm thickness, Silson Ltd, UK) were sterilized and placed in 6-well microplates. A2780 (ovarian) cancer cells were grown in RPMI 1640 medium (Roswell Park Memorial Institute; see below). The cell density required for one well was 22.5 × 10^4 cells in 3 mL to fully cover the window. The cell suspension was gently pipetted into each well and the plates were incubated for 36–40 h at 37 °C under a 5% CO_2 atmosphere for cells to grow and attach to the windows. Stock solutions (200 μM) of **1–4** in low glucose DMEM (Dulbecco's modified Eagle's medium) were diluted to 20 μM with DMEM (solution **4** contained 5% acetone for solubility purposes). RPMI medium was gently pipetted out, and the cells were treated with the 20 μM solution of each complex for 6 h. Those in control wells were treated with pure DMEM. After 6 h, the medium was removed, and the cells were washed with 3 mL of Dulbecco's PBS (D-PBS), followed by chemical fixation of the cells using a 4% paraformaldehyde solution in D-PBS, and incubation for 1 hour at 37 °C under a 5% CO_2 atmosphere. The windows were finally washed twice with 100 mM ammonium acetate solution in Milli-Q water and allowed to dry completely.

XFM data collection and data analysis. Single A2780 control cells and treated cells were imaged to obtain their elemental distribution maps on beamline 2-ID-D at the Advanced Photon Source (APS, 6 GeV and 160 mA), Argonne National Laboratory, Illinois, USA. Three to four individual cells for imaging were first selected using an optical microscope. The beam was tuned to an incident energy of 12.8 keV to allow for the excitation of the Re L-edge and the detection of the Re L_β emission line (E = 10 010.0 eV) as well as the fluorescence of lighter elements of interest (P, S, Ca, Cl, Cu, and Zn). The Re $L_{\beta1}$ emission line was used since its $L_{\alpha1}$ line (8652.5 eV) overlaps with the Zn $K_{\alpha1}$ emission line (8638.9 eV). The sample was positioned in the beam path with a 15° tilt, and a single element silicon drift detector (Vortex EX) was positioned at 90° to the beam. The incident beam spot size was focused to 0.35 μm × 0.35 μm using Fresnel zone plate focusing optics and elemental maps were collected in fly scan mode with a dwell time of 300 ms and a spatial resolution of 0.50 μm × 0.50 μm. For quantification (μg cm^{-2}), AXO (Dresden, Germany) thin film standards RF 19-200-S6247-09 were measured with the same sample and detector positions for comparison of fluorescence intensity. Data analysis was performed using the uProbeX program,[70] by first fitting the raw integrated spectrum of all pixels to the element emission energies, followed by per pixel processing, including the option for quantification to extract the fitted elemental maps and to quantify elemental concentrations. Contrast Re images were generated by setting a specific maximum concentration (μg cm^{-2}) across desired elemental maps. The mean maximum concentration, standard

deviations, and *p*-values were calculated using online calculators.[71,72]

Cell viability assay. The cytotoxicity of **1–4**, *fac*-[Re(CO)$_3$(GluP)Cl] and its hydrolyzed form *fac*-[Re(CO)$_3$(GluP)(H$_2$O)]Cl, as well as *fac*-[Re(CO)$_3$(GluQ)(H$_2$O)]Cl, the pure AcGluP ligand, and cisplatin was measured against four cancer cell lines A2780 (ovarian), MDA-MB-231 (breast), DU-145 (prostate), A459 (lung) and one primary cell line MRC-5 (lung) using the 3-[4,5-dimethylthiazol-2-yl]-2,5 diphenyl tetrazolium bromide (MTT) assay. For assays, the cells were trypsinized, counted to adjust for cell density, and seeded in 96-well flat-bottomed cell culture plates (KASVI) at a density of 1.5×10^4 cells per well. The plates were incubated at 37 °C with 5% CO_2 for 24 h for the attachment of cells to the wells. After this period, the culture medium was removed and 100 μL of fresh medium containing various concentrations of the complexes (ranging from 1.56 to 200 μM) was added. The plates were then incubated under the same conditions for 72 h. After incubation, 50 μL of MTT solution (1 mg mL^{-1} in PBS) was added to each well. The plates were further incubated for 3 h. During incubation, mitochondrial dehydrogenase in viable cells reduced the MTT and purple formazan crystals formed. These crystals were then solubilized by the addition of isopropanol, and the absorbance of each well was measured using a microplate reader (BioTek™, Epoch™) at a wavelength of 540 nm. The absorbance values were then used to determine the cytotoxicity of the complexes against different cell lines using GraphPad Prism Version 10.3 software. By fitting cell viability (%) *vs.* log [drug] curves, half-maximal inhibitory concentration (IC_{50}) values were calculated. All data were collected from nine replicates and the standard deviation was calculated.

Partition coefficient (log *P*). The partition coefficients of **1–4** were determined by the shake-flask method in water and *n*-octanol.[73] Complexes **1–3** were dissolved in pre-saturated water with *n*-octanol to give a $[C]_{init.water}$ = 50 μM solution, while **4** was dissolved in pre-saturated *n*-octanol with water to achieve $[C]_{init.oct}$ = 50 μM. The UV-vis spectra of the solutions were recorded to calculate the molar absorption coefficients (ε_{max}) using the Beer–Lambert law at the wavelength (λ_{max}) corresponding to the maximum absorption band of lowest energy: 377 nm (**1**), 367 nm (**2**), 403 nm (**3**), and 360 nm (**4**). Then a specific volume of each solution (**1–3**; V_{water}) was shaken with a known volume of pre-saturated *n*-octanol (V_{oct}) at three different v/v ratios 1 : 1, 1 : 2 and 2 : 1 for 30 minutes at room temperature. For **4**, this procedure was carried out by mixing a specific volume of its *n*-octanol solution (V_{oct}) with a known volume of pre-saturated water (V_{water}). After shaking, the water/*n*-octanol phases were separated by centrifuging the solutions at 3000 rpm for 5 min. The UV-vis absorption spectra of the aqueous phase for **1–3** and the *n*-octanol phase for **4** were recorded to determine the concentration of each corresponding complex remaining in solution after shaking: $[C]_{fin.water}$ for **1–3** and $[C]_{fin.oct}$ for **4**. The log *P* values of complexes **1–3** and **4** were calculated using eqn (1) and (2), respectively. The reported log *P* values are the average of three independent measurements, *i.e.* V_{water} (mL) : V_{oct} (mL) = 15 : 15, 7.5 : 15 and 15 : 7.5

$$\log P_{1-3} = \log\left[\frac{[C]_{init.water} - [C]_{fin.water}}{[C]_{fin.water}} \times \frac{V_{water}}{V_{oct}}\right] \quad (1)$$

$$\log P_4 = \log\left[\frac{[C]_{init.oct} - [C]_{fin.oct}}{[C]_{fin.oct}} \times \frac{V_{water}}{V_{oct}}\right] \quad (2)$$

Author contributions

The manuscript was written by B. A. and F. J. All authors contributed to data collection and/or data analysis and approved the final version of the manuscript.

Conflicts of interest

There are no conflicts to declare.

Data availability

The data supporting this article have been included as part of the supplementary information (SI). Supplementary information: further experimental details, ^{1}H-, ^{13}C-NMR, and 2D NMR spectra (HSQC), FT-IR spectra and analysis of vibrational bands, time study NMR, UV-vis and ESI-mass spectra, details of theoretical calculations and GC-TCD measurements of released CO, cellular uptake, cell viability, cell morphological and clonogenic assays,and additional XFM images of cells (treated *vs.* control), as well as the atomic coordinates for the optimized ground state sructures. See DOI: https://doi.org/10.1039/d6dt00710d.

Acknowledgements

We would like to express our deepest appreciation to Dr Veronika Pape, Professor Hugh Harris and Meaghan Ashton (University of Adelaide) for the HepG2 cellular uptake measurements, and our sincere gratitude to Professors Chang-Chun Ling and Roland Roesler (University of Calgary) for their insightful discussions. We are grateful to the staff, especially to Dr Michelle Thibault at the Instrumentation Facility, Department of Chemistry, University of Calgary, and to Dr Amani M. Ebrahim, at the BioXAS-Main beamline, the Canadian Light Source. We also acknowledge the awarded X-ray absorption spectroscopy beam times at the BioXAS-Main beamline at the Canadian Light Source (CLS; proposal number: 39G13890), beamline 12C at the Photon Factory, High Energy Accelerator Research Organization (PF- KEK; proposal number: 2025G639), and X-ray fluorescence microscopy data collected at the 2-ID-D beamline at the Advanced Photon Source (APS; proposal number: 1012080 and 1018407). This research was performed using the APS beam time award

(https://doi.org/10.46936/APS-192373/60015877, https://doi.org/10.46936/APS-191786/60015494) from the Advanced Photon Source, a U.S. Department of Energy (DOE) Office of Science user facility operated for the DOE Office of Science by the Argonne National Laboratory under Contract No. DE-AC02-06CH11357. Some of the Office of Science support comes from Biological and Environmental Research (BER). Part of the research described in this paper was performed using the awarded beam time at the Canadian Light Source, a national research facility of the University of Saskatchewan, which is supported by the Canada Foundation for Innovation (CFI), the Natural Sciences and Engineering Research Council (NSERC), the Canadian Institutes of Health Research (CIHR), the Government of Saskatchewan, and the University of Saskatchewan. This research was financially supported by the Natural Sciences and Engineering Research Council of Canada (NSERC) funding reference numbers RGPIN 2016-04546 and RGPIN 2022-02996, Mitacs through the Mitacs Globalink Research Award Program (application reference IT44014), the Canada Foundation for Innovation (Grant no. 9479) and the Province of Alberta – Department of Innovation and Science. Theoretical calculations were performed using the computer resources provided by the Digital Research Alliance of Canada (https://www.alliancecan.ca) and Prairies DRI (Digital Research Infrastructure). FJ acknowledges the scholarship from the Global Affairs Canada – Faculty Mobility for Partnership Building Program (project number: FMPB-2025-GA-1-University of Calgary).

References

1 S. Ghosh, *Bioorg. Chem.*, 2019, **88**, 102925.
2 S. M. Cohen and S. J. Lippard, in *Progress in Nucleic Acid Research and Molecular Biology*, 2001, vol. 67, pp. 93–130.
3 D. Screnci, M. J. McKeage, P. Galettis, T. W. Hambley, B. D. Palmer and B. C. Baguley, *Br. J. Cancer*, 2000, **82**, 966–972.
4 K. M. Deo, D. L. Ang, B. McGhie, A. Rajamanickam, A. Dhiman, A. Khoury, J. Holland, A. Bjelosevic, B. Pages, C. Gordon and J. R. Aldrich-Wright, *Coord. Chem. Rev.*, 2018, **375**, 148–163.
5 C. Zhang, C. Xu, X. Gao and Q. Yao, *Theranostics*, 2022, **12**, 2115–2132.
6 V. Tomar, P. Kumar, D. Sharma, R. K. Joshi and M. Nemiwal, *J. Mol. Struct.*, 2025, **1319**, 139589.
7 E. Alessio and L. Messori, *Molecules*, 2019, **24**, 1995.
8 M. Rausch, P. J. Dyson and P. Nowak-Sliwinska, *Adv. Ther.*, 2019, **2**, 1900042.
9 S. M. Meier, M. Hanif, Z. Adhireksan, V. Pichler, M. Novak, E. Jirkovsky, M. A. Jakupec, V. B. Arion, C. A. Davey, B. K. Keppler and C. G. Hartinger, *Chem. Sci.*, 2013, **4**, 1837–1846.
10 A. Amaya-Florez, J. R. Galindo, E. Sanchez-Yocue, A. Ruiz-Martinez, J. S. Serrano-Garcia, A. Romo-Perez, P. Cano-Sanchez, V. Reyes-Marquez, R. Le Lagadec and D. Morales-Morales, *RSC Med. Chem.*, 2025, **16**, 5125–5195.
11 G. Bernal, G. Aquea and S. Ramirez-Rivera, *Oncol. Res.*, 2025, **33**, 759–779.
12 A. Kumar Singh, A. Kumar, H. Singh, P. Sonawane, P. Pathak, M. Grishina, J. Pal Yadav, A. Verma and P. Kumar, *Chem. Biodivers.*, 2023, **20**, e202300061.
13 N. Muhammad, M. Hanif and P. Yang, *Coord. Chem. Rev.*, 2024, **499**, 215507.
14 M. G. Vander Heiden, L. C. Cantley and C. B. Thompson, *Science*, 2009, **324**, 1029–1033.
15 S. Ben-Haim and P. Ell, *J. Nucl. Med.*, 2009, **50**, 88–99.
16 Y. Mikata, Y. Shinohara, K. Yoneda, Y. Nakamura, I. Brudziñska, T. Tanase, T. Kitayama, R. Takagi, T. Okamoto, I. Kinoshita, M. Doe, C. Orvig and S. Yano, *Bioorg. Med. Chem. Lett.*, 2001, **11**, 3045–3047.
17 M. Patra, T. C. Johnstone, K. Suntharalingam and S. J. Lippard, *Angew. Chem., Int. Ed.*, 2016, **55**, 2550–2554.
18 M. Patra, S. G. Awuah and S. J. Lippard, *J. Am. Chem. Soc.*, 2016, **138**, 12541–12551.
19 K. Ling, F. Men, W. C. Wang, Y. Q. Zhou, H. W. Zhang and D. W. Ye, *J. Med. Chem.*, 2018, **61**, 2611–2635.
20 S. Bonnet, *Dalton Trans.*, 2018, **47**, 10330–10343.
21 J. J. Wilson, in *Advances in Inorganic Chemistry*, ed. P. C. F. A. R. V. Eldik, Academic Press, 2022, vol. 80, pp. 1–33.
22 L. E. Enslin, K. Purkait, M. D. Pozza, B. Saubamea, P. Mesdom, H. G. Visser, G. Gasser and M. Schutte-Smith, *Inorg. Chem.*, 2023, **62**, 12237–12251.
23 J. Yang, J. X. Zhao, Q. Cao, L. Hao, D. Zhou, Z. Gan, L. N. Ji and Z. W. Mao, *ACS Appl. Mater. Interfaces*, 2017, **9**, 13900–13912.
24 R. Alberto, R. Schibli, A. Egli, P. A. Schubiger, W. A. Herrmann, G. Artus, U. Abram and T. A. Kaden, *J. Organomet. Chem.*, 1995, **493**, 119–127.
25 S. Sato, T. Morimoto and O. Ishitani, *Inorg. Chem.*, 2007, **46**, 9051–9053.
26 W. Wang, B. Spingler and R. Alberto, *Inorg. Chim. Acta*, 2003, **355**, 386–393.
27 W. Beck, W. Hieber and G. Braun, *Z. Anorg. Allg. Chem.*, 1961, **308**, 23–32.
28 B. Abdolahi Sanati, T. S. B. Trung, D. Bonnaventure, A. M. Ebrahim, A. Rauk and F. Jalilehvand, *Inorg. Chem.*, 2025, **64**, 16347–16360.
29 B. Salignac, P. V. Grundler, S. Cayemittes, U. Frey, R. Scopelliti and A. E. Merbach, *Inorg. Chem.*, 2003, **42**, 3516–3526.
30 S. C. Marker, A. P. King, S. Granja, B. Vaughn, J. J. Woods, E. Boros and J. J. Wilson, *Inorg. Chem.*, 2020, **59**, 10285–10303.
31 C. C. Konkankit, J. Lovett, H. H. Harris and J. J. Wilson, *Chem. Commun.*, 2020, **56**, 6515–6518.
32 Z. Y. Pan, C. P. Tan, L. S. Rao, H. Zhang, Y. Zheng, L. Hao, L. N. Ji and Z. W. Mao, *Angew. Chem., Int. Ed.*, 2020, **59**, 18755–18762.
33 R. R. Ye, B. C. Chen, J. J. Lu, X. R. Ma and R. T. Li, *J. Inorg. Biochem.*, 2021, **223**, 111537.
34 L. He, Z. Y. Pan, W. W. Qin, Y. Li, C. P. Tan and Z. W. Mao, *Dalton Trans.*, 2019, **48**, 4398–4404.

35 S. F. He, N. L. Pan, B. B. Chen, J. X. Liao, M. Y. Huang, H. J. Qiu, D. C. Jiang, J. J. Wang, J. X. Chen and J. Sun, *J. Biol. Inorg. Chem.*, 2020, **25**, 1107–1116.
36 G. Bononi, D. Iacopini, G. Cicio, S. Di Pietro, C. Granchi, V. Di Bussolo and F. Minutolo, *ChemMedChem*, 2021, **16**, 30–64.
37 T. Storr, M. Obata, C. L. Fisher, S. R. Bayly, D. E. Green, I. Brudzinska, Y. Mikata, B. O. Patrick, M. J. Adam, S. Yano and C. Orvig, *Chem. Eur. J.*, 2005, **11**, 195–203.
38 S. Mal, U. Malik, M. Mahapatra, A. Mishra, D. Pal and S. K. Paidesetty, *Drug Dev. Res.*, 2022, **83**, 1469–1504.
39 BOLD-100 Plus Doxorubicin in Advanced Soft Tissue Sarcomas. ClinicalTrials.gov identifier: NCT07027423, https://clinicaltrials.gov/study/NCT07027423?intr=KP1339&viewType=Card&rank=1, (accessed 2026-04-27).
40 BOLD-100 in Combination With FOLFOX for the Treatment of Advanced Solid Tumours. ClinicalTrials.gov identifier: NCT04421820, https://clinicaltrials.gov/study/NCT04421820?intr=KP1339&viewType=Card&rank=2, (accessed 2026-04-27).
41 E. Jortzik, M. Farhadi, R. Ahmadi, K. Toth, J. Lohr, B. M. Helmke, S. Kehr, A. Unterberg, I. Ott, R. Gust, V. Deborde, E. Davioud-Charvet, R. Reau, K. Becker and C. Herold-Mende, *Biochim. Biophys. Acta*, 2014, **1844**, 1415–1426.
42 O. Shengju, Z. Lin, C. Duan, H. Zhang and Z. Bai, *Chem. Commun.*, 2006, 4392–4394.
43 B. C. E. Makhubela, A. Jardine and G. S. Smith, *Appl. Catal., A*, 2011, **393**, 231–241.
44 G. Cerchiaro, F. R. Bertuchi and C. M. L. Machado, Cupric complex, pharmaceutical composition and use of the cupric complex Brazil Pat., BR102020014663-7A, 2022.
45 C. M. A. M. Parrinello, *J. Am. Chem. Soc.*, 1998, **120**, 2168–2171.
46 E. Matamoros, E. M. S. Perez, M. E. Light, P. Cintas, R. F. Martinez and J. C. Palacios, *J. Org. Chem.*, 2024, **89**, 7877–7898.
47 J. Reedijk, *Recl. Trav. Chim. Pays-Bas*, 2010, **88**, 1451–1470.
48 G. R. Fulmer, A. J. M. Miller, N. H. Sherden, H. E. Gottlieb, A. Nudelman, B. M. Stoltz, J. E. Bercaw and K. I. Goldberg, *Organometallics*, 2010, **29**, 2176–2179.
49 P. K. Glasoe and F. A. Long, *J. Phys. Chem.*, 1960, **64**, 188–190.
50 F. Jalilehvand, A. Enriquez Garcia and P. Niksirat, *ACS Omega*, 2017, **2**, 6174–6186.
51 A. A. Abramov, A. I. Zinin, N. G. Kolotyrkina, L. O. Kononov, A. Shatskiy, M. D. Kärkäs and E. V. Stepanova, *J. Org. Chem.*, 2024, **89**, 10021–10026.
52 M. Y. Moridani, in *Prodrugs and Targeted Delivery: Towards Better ADME Properties*, ed. J. Rautio, Wiley VCH, Weinheim, Germany, 2010, ch. 4, pp. 81–109.
53 J. A. Arnott and S. L. Planey, *Expert Opin. Drug Discovery*, 2012, **7**, 863–875.
54 X. Liu, B. Testa and A. Fahr, *Pharm. Res.*, 2011, **28**, 962–977.
55 V. Fernandez-Moreira, F. L. Thorp-Greenwood and M. P. Coogan, *Chem. Commun.*, 2010, **46**, 186–202.
56 Cell line - SLC2A1 - The Human Protein Atlas., https://www.proteinatlas.org/ENSG00000117394-SLC2A1/cell+line (accessed 2026-01-02).
57 M. Cassandri, A. Smirnov, F. Novelli, C. Pitolli, M. Agostini, M. Malewicz, G. Melino and G. Raschella, *Cell Death Discovery*, 2017, **3**, 17071.
58 G. Wu, Y. Z. Fang, S. Yang, J. R. Lupton and N. D. Turner, *J. Nutr.*, 2004, **134**, 489–492.
59 M. S. Capper, A. Enriquez Garcia, N. Macia, B. Lai, J. B. Lin, M. Nomura, A. Alihosseinzadeh, S. Ponnurangam, B. Heyne, C. S. Shemanko and F. Jalilehvand, *J. Biol. Inorg. Chem.*, 2020, **25**, 759–776.
60 N. Atale, S. Gupta, U. C. Yadav and V. Rani, *J. Microsc.*, 2014, **255**, 7–19.
61 F. Doonan and T. G. Cotter, *Methods*, 2008, **44**, 200–204.
62 J. J. Manura and D. J. Manura, Scientific Instrument Services (SIS): Isotope Distribution Calculator and Mass Spec Plotter, https://www.sisweb.com/mstools/isotope.htm.
63 T. D. W. Claridge, in *High-Resolution NMR Techniques in Organic Chemistry*, ed. T. D. W. Claridge, Elsevier, 3 edn, 2016, ch. 3, pp. 61–132.
64 *The Merck Index: An Encyclopedia of Chemicals, Drugs, and Biologicals*, eds. M. J. O'Neil, P. E. Heckelman, C. B. Koch and K. J. Roman, Merck, John Wiley & Sons Inc., Hoboken, NJ, 14th edn, 2006.
65 B. Ravel and M. Newville, *J. Synchrotron Radiat.*, 2005, **12**, 537–541.
66 T. Ressler, *J. Synchrotron Radiat.*, 1998, **5**, 118–122.
67 B. Ravel, *J. Synchrotron Radiat.*, 2000, **8**, 314–316.
68 S. I. Zabinsky, J. J. Rehr, A. Ankudinov, R. C. Albers and M. J. Eller, *Phys. Rev. B:Condens. Matter Mater. Phys.*, 1995, **52**, 2995–3009.
69 A. L. Ankudinov and J. J. Rehr, *Phys. Rev. B:Condens. Matter Mater. Phys.*, 1997, **56**, R1712–R1715.
70 A. Glowacki, Aglowacki/uProbeX, 2026, https://github.com/aglowacki/uProbeX, (accessed 2026-02-19).
71 E. Furey, *Descriptive Statistics Calculator*, https://www.calculatorsoup.com/calculators/statistics/descriptivestatistics.php, from CalculatorSoup, https://www.calculatorsoup.com - Online Calculators (accessed 2026-03-09).
72 *T* test calculator, https://www.graphpad.com/quickcalcs/ttest1/, (accessed 2026-03-09).
73 OECD, Test No. 107: Partition Coefficient (*n*-octanol/water): Shake Flask Method, OECD Guidelines for the Testing of Chemicals, Section 1, Paris, 1995.